ACCSCIENCE PUBLISHING

International Journal of Bioprinting

RESEARCH ARTICLE

Low-density ZIF-8 coating optimizes the immune microenvironment of 3D-printed PCL scaffolds and promotes cranial defect repair

Qianyu Xie[1,2†], Xusihong Cai[1,2,3†], Guangquan Zhao[1,2†], Hao Tang[1], Yuanhao Lv[1,2], Jiaxiang Song[1], Shuai Huang[4*], Weikang Xu[2,4*], and Qingde Wa[1*]

[1]Department of Orthopedic Surgery, The Second Affiliate Hospital of Zunyi Medical University, Zunyi, Guizhou, China

[2]Institute of Biological and Medical Engineering, Guangdong Academy of Sciences, Guangzhou, Guangdong, China

[3]Department of Nursing, Nursing School of Zunyi Medical University, Zunyi Medical University, Zunyi, Guizhou, China

[4]National Engineering Research Center for Healthcare Devices, Guangdong Provincial Key Laboratory of Medical Electronic Instruments and Materials, Guangdong Institute of Medical Instruments, Guangzhou, Guangdong, China

[†]*These authors contributed equally to this work.*

***Corresponding authors:**
Qingde Wa
(wqd887zsy@126.com)
Weikang Xu
(759200816@qq.com)
Shuai Huang
(huangshuai316@163.com)

Citation: Xie Q, Cai X, Zhao G, *et al*. Low-density ZIF-8 coating optimizes the immune microenvironment of 3D-printed PCL scaffolds and promotes cranial defect repair. *Int J Bioprint*. 2026;12(3):026170150. doi: 10.36922/IJB026170150

Received: April 2, 2026

Revised: May 13, 2026

Accepted: May 14, 2026

Published online: May 18, 2026

Abstract

The hydrophobicity of 3D-printed polycaprolactone (PCL) scaffolds leads to insufficient cell adhesion, limiting their application in bone repair. This study constructed zeolitic imidazolate framework-8 (ZIF-8) modified PCL scaffolds with different coating densities and systematically evaluated their physicochemical properties and osteogenic effects. The results showed that low-density ZIF-8-coated PCL scaffolds exhibited better biocompatibility and osteogenic differentiation promotion capacity, while maintaining structural stability and mechanical properties. Mechanistically, the low-density coating can induce macrophages toward M2 polarization, thereby forming a more favorable osteogenic immune microenvironment. Simultaneously, in a rat skull defect model, this scaffold significantly promoted new bone regeneration and defect repair. This study indicates that ZIF-8 coating density is a key parameter affecting the immunomodulatory osteogenic efficacy of PCL scaffolds, providing a basis for the design and optimization of metal–organic framework-based coated scaffolds.

Keywords: 3D-printed scaffold; Polycaprolactone; Zeolitic imidazolate framework-8; Macrophage polarization; Bone regeneration

1. Introduction

Bone defects refer to the destruction of bone integrity caused by skeletal diseases such as trauma, infection, bone tumors, congenital developmental disorders, and osteoporosis.[1,2] Although bone tissue has a certain self-repairing ability, severe bone defects can lead to loss of bone function and failure to heal, often requiring surgery and bone grafting to induce bone regeneration.[3] Autologous bone graft is considered the "gold standard" for treating bone defects, but its supply is limited.[4,5] In recent years, with the development

of tissue engineering, the application of biomaterials in the field of bone defect repair has received increasing attention, and bone repair substitutes prepared based on biomaterials have provided a new treatment strategy for bone defects.[6,7] Favorable mechanical properties, high biocompatibility, and potent osteogenic inductive ability are the basic requirements for bone graft materials.[8,9] The process of bone defect repair involves complex immune responses, in which macrophages play a key immunoregulatory role.[10] M1 and M2 macrophages can secrete different cytokines to regulate bone repair, and the macrophage phenotype can switch in different microenvironments.[11] M1 macrophages secrete a variety of pro-inflammatory factors, which lead to chronic inflammatory responses. M2 macrophages can produce a variety of anti-inflammatory cytokines to alleviate inflammation and enhance osteogenic activity.[12] Therefore, exploring bone repair materials with the ability to regulate the immune microenvironment can improve the biocompatibility of biomaterials with human tissues and promote the repair of bone defects.

Polycaprolactone (PCL) is a synthetic biodegradable polyester with high plasticity, a low melting point, and ease of processing. It also has high biocompatibility with various tissues in the body, and its degradation products are non-toxic to the human body, reducing immune responses. It is often used in three-dimensional (3D) printing to design bone scaffolds to provide support for tissue regeneration.[13,14] Because PCL is derived from ε-caprolactone, its repeating unit can be represented as $-(O-(CH_2)_5-CO)_n-$, which contains both polar ester bonds (–COO–) and nonpolar methylene chains ($-(CH_2)_5-$). The relatively long nonpolar methylene segment in the PCL repeating unit makes the polymer predominantly hydrophobic, which reduces cell adhesion on pure PCL scaffolds. This results in low cell affinity of pure PCL scaffolds, which is not conducive to cell adhesion and limits the bone repair process.[15,16] Therefore, in the biomedical field, surface modification techniques are often used to coat the surface of PCL scaffolds with other materials to improve them.[17,18]

Among them, zeolitic imidazolate framework-8 (ZIF-8) is a metal–organic framework (MOF) material formed by the self-assembly of zinc nitrate hexahydrate and 2-methylimidazole. Its synthesis is mainly achieved through a simple solution method.[19] Due to the wide range of physical and mechanical properties and structural flexibility of MOF materials, the introduction of ZIF-8 as a surface modification material can significantly improve the surface roughness of traditional materials and enhance cell adhesion rate.[20] ZIF-8 degrades slowly in the physiological environment, continuously releasing zinc ions (Zn^{2+}). The released Zn^{2+} effectively kills bacteria (such as *Streptococcus mutans*), creating a clean local environment for bone regeneration.[21] Studies have shown that Zn^{2+} can directly stimulate osteoblast activity, inhibit osteoclasts, and synergistically promote bone defect repair.[22] For example, Tian *et al.*[23] used plasma immersion ion implantation and deposition technology to introduce Zn^{2+} onto the surface of pure titanium, confirming that implants with introduced Zn^{2+} have the ability to promote osteogenesis and osteointegration in the early stages of bone grafting. ZIF-8 exhibits excellent cytocompatibility and can promote immune-regulated bone repair performance.[24] Recent studies have shown that ZIF-8 hydrogel exhibits good biocompatibility both *in vitro* and *in vivo*. Si *et al.*[25] found that ZIF-8 composite hydrogel encapsulated by exosomes can inhibit the activation of the non-canonical NF-κB pathway in RAW264.7 cells, thereby downregulating the expression of pro-inflammatory cytokines and inducing RAW264.7 cells to polarize towards the M2 phenotype, thus establishing an immune microenvironment conducive to osteogenic formation *in vivo*, and significantly promoting new bone formation and angiogenesis. However, ZIF-8 nanomaterials still face significant challenges, as excessive release of Zn^{2+} may relatively reduce biological performance.[26] Furthermore, studies have shown that excessive Zn^{2+} release may impair early cell responses and mitochondrial function, leading to the production of large amounts of reactive oxygen species (ROS). Excessive ROS accumulation can cause oxidative damage to cells and ultimately cell death.[27]

Although ZIF-8, as a typical MOF material, has been extensively studied in fields such as drug delivery and catalysis, its application as a surface functional coating material has rarely been reported in previous literature. Therefore, the primary novelty of this work lies in establishing ZIF-8 as a surface functional coating and conducting its comprehensive characterization. This study used ZIF-8 coatings of different densities as surface modifiers to modify the surface of 3D-printed PCL scaffolds. It explored the biocompatibility, osteogenic induction, effects of regulating macrophage polarization on the bone immune microenvironment, and cranial defect repair effects of PCL scaffolds coated with ZIF-8 of different densities. This provides a basis for the design and optimization of MOF-based coated scaffolds.

A schematic diagram of the overall study design is shown in Figure 1.

2. Materials and methods

2.1. Materials

Materials used in this study included: a scanning electron microscope (SEM; Phenom ProX, Netherlands), an energy

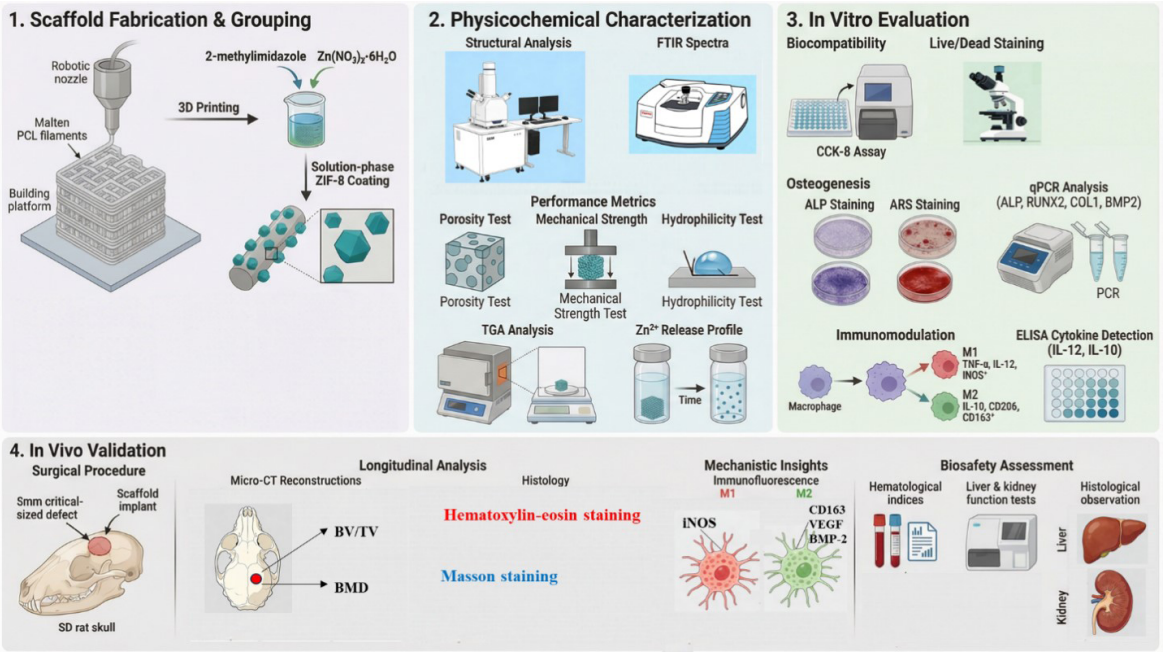

Figure 1. Schematic diagram of the study design

Abbreviations: ALP: Alkaline phosphatase; ARS: Alizarin Red S; BMD: Bone mineral density; BMP2: Bone morphogenetic protein-2; BV/TV: Bone volume fraction; CD163: Hemoglobin scavenger receptor; CD206: Differentiation cluster 206 (mannose receptor); COL1: Type I collagen; FTIR: Fourier transform infrared spectroscopy; IL: Interleukin; iNOS: Inducible nitric oxide synthase; PCL: Polycaprolactone; RUNX2: Runt-related transcription factor 2; SEM: Scanning electron microscope; TGA: Thermogravimetric analyzer; TNF-α: Tumor necrosis factor-α; VEGF: Vascular endothelial growth factor; ZIF-8: Zeolitic imidazolate framework-8.

dispersive spectroscopy (EDS) spectrometer (Phenom ProX, Thermo Scientific, Netherlands), a Fourier transform infrared spectrometer (iS™ 20 FTIR, Thermo, China), a micro-computed tomography (CT) scanner (μCT 35, Scanco, Switzerland), a fluorescence microscope (Olympus IX51, Olympus, Japan), and a universal testing machine (INSTRON 34SC-05, Instron, United States of America [USA]). 2-Methylimidazole and zinc nitrate hexahydrate were purchased from Shanghai Maclean Biotechnology Co., Ltd., China. PCL (molecular weight: 48,000) was purchased from Jinan Daigang Biotechnology Co., Ltd, China. RNA extraction kits and reverse transcription kits were purchased from CWBIO (CW0581S, China). CCK-8 assay kit (C0037), cell viability assay kit (C2015S), alkaline phosphatase (ALP) kit (P0321 M), BCA protein assay kit (P0012), osteoblast mineralization nodule staining kit (C0148S), hematoxylin and eosin (HE) staining kit (C0105S), and Masson's trichrome staining kit (C0189S) were provided by Beyotime Biotechnology Co., Ltd (Shanghai, China). Enzyme-linked immunosorbent assay (ELISA) kit (IL-10 [EM220162], IL-12 [EM220166]) were procured from BYabscience (China) Dulbecco's modified Eagle medium (DMEM), fetal bovine serum, penicillin-streptomycin solution, phosphate-buffered saline, and trypsin were all purchased from Gibco (USA). Rat bone marrow mesenchymal stem cells (BMSCs) and macrophages (RAW264.7) were obtained from ATCC (USA).

2.2. Scaffold preparation

After thorough drying, PCL particles were placed in a printing cartridge and then loaded into a 3D printer. The printing nozzle diameter was 0.5 mm. The parameters were set as follows: cartridge temperature 70 °C, nozzle temperature 70 °C, fiber spacing 1.0 mm × 1.0 mm, printing speed 10 mm/s, fiber orientation 0–90°, and air pressure 100 kPa. After setting these parameters, the printhead was started, producing a cylindrical PCL scaffold.

To prepare ZIF-8-coated PCL scaffolds, 0.165 g of 2-methylimidazole was dissolved in 50 mL of deionized water under stirring. Separately, 0.075 g of zinc nitrate hexahydrate was dissolved in 25 mL of deionized water under stirring. The prepared PCL scaffolds were completely immersed in a 2-methylimidazole solution, after which the zinc nitrate solution was added dropwise under magnetic stirring. The reaction was continued for four hours. Unbound ZIF-8 particles were removed by rinsing the scaffolds with deionized water, and the scaffolds were

then dried in a vacuum oven at 50 °C to obtain low-density ZIF-8-coated PCL scaffolds (LZPs). High-density ZIF-8-coated PCL scaffolds (HZP) were prepared using the same procedure, except that 0.825 g of 2-methylimidazole and 0.375 g of zinc nitrate hexahydrate were used.

2.3. Scaffold characterization

2.3.1. Surface morphology

To study the surface morphology characteristics of the three scaffolds, the surface morphology was characterized using scanning electron microscopy. Gold was sputtered onto the scaffold surface, and the microstructure and structure of the scaffolds were observed using scanning electron microscopy at an accelerating voltage of 10 kV.

2.3.2. Elemental composition

To determine the elemental composition of the scaffold surface, EDS analysis was performed. Gold was sputtered onto the surface of the scaffold, and the microstructure and structure of the scaffold were observed using a scanning electron microscope under an accelerating voltage of 10 kV.

2.3.3. Scaffold porosity

The mass of the dried scaffold sample was recorded as M0, and the total mass of the specific gravity bottle containing anhydrous ethanol at room temperature was recorded as M1. The scaffold sample was then placed in the specific gravity bottle and ultrasonicated for 10 min to remove air bubbles. The total mass of the sample was recorded as M2. After the scaffold sample was removed, the mass of the remaining sample was recorded as M3. The porosity of the scaffold was calculated using the following formula:

$$P = (M2 - M3 - M0) / (M1 - M3) \quad (1)$$

2.3.4. X-ray diffraction

X-ray diffraction (XRD) was used to characterize the crystalline structure of the ZIF-8 particles. The scanning angle ranged from 5° to 90°, with a scanning speed of 2°/min.

2.3.5. Scaffold mechanical strength

The cylindrical scaffold specimens (diameter 5 mm × height 10 mm) were placed on a universal testing machine to evaluate their mechanical properties. The extrusion speed was set to 5 mm/min. Based on the cross-sectional area of the scaffold, the peak load was converted into compressive strength, and the equipment automatically recorded the corresponding compression modulus. The test was performed in triplicate, and stress–strain curves were plotted for the scaffold specimens.

2.3.6. Scaffold hydrophilicity

The hydrophilicity of the scaffolds was evaluated using the water droplet method. The scaffolds were fixed on the sample stage of the DSA2S contact angle analysis system (KRÜSS Drop Shape Analyzer DSA100, KRÜSS GmbH, Germany). A 2-μL droplet of ultrapure water was vertically added 2 mm from the sample using a microsyringe. The droplet morphology at the moment of contact was captured by a high-speed camera, and the contact angle measurement software automatically calculated the contact angle.

2.3.7. Chemical composition

The chemical composition of the three scaffolds was characterized using Fourier Transform Infrared Spectroscopy (FTIR). The vacuum-dried scaffolds were ground into powder, and the sample powder was then pressed into thin sheets. The spectral range was 800–4000 cm^{-1}, and data were plotted.

2.3.8. Thermogravimetric analysis

Thermogravimetric analysis was used to determine the thermogravimetric data of three groups of scaffolds. The scaffolds were prepared into uniform particles or powders. The samples were heated from room temperature to 800 °C at a rate of 10 °C/min under nitrogen protection, and the mass change of the samples was continuously monitored.

2.3.9. In vitro ion release

Inductively coupled plasma optical emission spectroscopy was used to measure Zn^{2+} release from two groups of ZIF-8-coated scaffolds. The scaffolds were immersed in 5 mL phosphate-buffered saline (PBS), and the concentration of Zn^{2+} in the PBS solution was measured on days 1, 3, 7, and 14, and the data were plotted.

2.4. *In vitro* experiments

2.4.1. Thawing and passaging of bone marrow mesenchymal stem cells and RAW264.7 cells

Cryovials containing BMSCs and RAW264.7 cells stored in liquid nitrogen were removed and thawed in a 37 °C water bath. The cell suspension was transferred to a 15-mL sterile centrifuge tube, mixed with 3 mL of complete culture medium, and centrifuged at low speed (1,000 rpm, 5 min). The supernatant was aspirated, and the cell pellet was resuspended in 2 mL of complete culture medium. The cell suspension was then transferred to a new culture flask, supplemented with 10 mL of complete culture

medium, gently mixed, and incubated at 37 °C in a 5% CO_2 incubator. The cells were passaged when they reached approximately 80–90% confluence. For scaffold-based assays, BMSCs were detached using trypsin, resuspended in culture medium to prepare a cell suspension, and seeded onto the scaffolds at a density of 1×10^5 cells/cm^2.

2.4.2. Scaffold sterilization

Before the experiment, the scaffolds were sterilized by soaking in 75% alcohol for 2 hours, followed by washing the scaffolds three times with PBS. After overnight UV irradiation, the scaffolds were washed three more times with PBS and then immersed in complete culture medium for 24 hours for later use.

2.4.3. CCK-8 assay for cell proliferation

The sterilized scaffold samples were placed in 48-well plates. BMSCs were seeded onto the scaffolds as described in Section 2.4.1. After culturing for 1, 3, and 7 days, the supernatant was aspirated, and 200 μL of CCK-8 working solution was added to each well. A blank control well containing only CCK-8 working solution and no cells was also included for background correction. The cells were incubated at 37 °C in a 5% CO_2 incubator for 2 h in the dark. The absorbance (OD value) at 450 nm was measured using a multi-mode microplate reader (Tecan Spark, Tecan Austria GmbH, Austria) to assess the cell proliferation capacity of each scaffold.

2.4.4. Live/dead cell fluorescent staining

Sterilized scaffold samples were placed in 48-well plates. BMSCs were seeded onto the scaffolds as described in Section 2.4.1. After three days of culture, the supernatant was aspirated, and Calcein AM/PI working solution (Beyotime Biotechnology Co., Ltd, China) was added for staining in the dark. Images were taken under an inverted fluorescence microscope to observe the state and distribution of cells on the scaffold surface.

2.4.5. Alkaline phosphatase staining and quantitative analysis

Bone marrow mesenchymal stem cells were seeded onto the scaffolds as described in Section 2.4.1 and cultured in osteogenic medium. On day 7 of culture, osteogenic medium was removed, and the cells were washed with PBS, fixed with 4% paraformaldehyde for 2 min, and then washed with PBS. For the ALP detection assay, 400 μL of BCIP/NBT staining working solution was added to each well, and the cells were incubated at room temperature in the dark for 30 min. The staining reaction was terminated by washing twice with distilled water, and the cells were observed, and images were acquired under a microscope.

For quantitative analysis, the osteogenic culture medium was removed, and the adherent BMSCs were lysed using cell lysis buffer. The lysis buffer was mixed with the ALP detection substrate solution at a 1:1 ratio, incubated at 37 °C for 30 min, and the reaction was terminated by adding the reaction stop solution. The OD value was measured at 405 nm using a multi-mode microplate reader. The total protein content of the cell lysis buffer was determined using the BCA method, and ALP activity was expressed as the measured OD value divided by the total protein content.

2.4.6. Calcium nodule staining and quantitative analysis

Bone marrow mesenchymal stem cells were seeded onto the scaffolds as described in Section 2.4.1 and cultured in osteogenic medium. On day 14 of culture, the osteogenic medium was removed, and the scaffolds were rinsed with PBS, fixed with 4% paraformaldehyde for 2 min, and washed again with PBS. Alizarin Red S staining solution (Beyotime Biotechnology Co., Ltd, China) was added to submerge the scaffolds, and staining was performed at room temperature for 30 min. After staining and air-drying, the stained scaffolds were observed, and images were acquired under a microscope.

After staining, the calcium nodules on the scaffolds were fully dissolved in 10% cetylpyridinium chloride solution, and the OD value was measured at 562 nm using a multi-mode microplate reader to quantify the calcium nodules on each group of scaffolds.

2.4.7. Detection of osteogenesis-related gene expression

Bone marrow mesenchymal stem cells were seeded onto the scaffolds as described in Section 2.4.1 and cultured in osteogenic medium. After osteogenic induction for 7 and 14 days, real-time quantitative polymerase chain reaction (RT-qPCR) was used to detect the expression of osteogenic marker genes, including ALP (*Alpl*), Runt-related transcription factor 2 (*Runx2*), collagen type I alpha 1 chain (*Col1a1*), and bone morphogenetic protein 2 (*Bmp2*), with glyceraldehyde-3-phosphate dehydrogenase (*Gapdh*) used as the internal control gene.

2.4.8. Detection of macrophage polarization gene and protein expression

RAW264.7 cells were seeded on scaffolds at a density of 1×10^5 cells/cm^2 and cultured in osteogenic medium. After culturing for 1 and 3 days, the expression of the M1 immunomarker genes tumor necrosis factor-α (*Tnfa*) and interleukin-1β (*Il1b*) and the M2 immunomarker genes *Cd206* and arginase (*Arg1*) were detected by RT-qPCR, with *Gapdh* used as an internal control gene.

After culturing for 1 and 3 days, the levels of interleukin-10 (IL-10) and interleukin-12 (IL-12) were detected using ELISA. The absorbance (optical density [OD] value) was measured at 450 nm using a multi-mode microplate reader.

2.5 *In vivo* experiments

2.5.1. Animal experiments and grouping and statement of ethics

A total of 36 healthy Sprague–Dawley (SD) rats (over 8 weeks old, male, weighing 280–310g) were used in this study. The rats were randomly divided into control, PCL, LZP, and HZP groups, with nine rats in each group. The experimental animals were housed under the same conditions in the animal facility of the Animal Experiment Center of Zunyi Medical University. All experimental protocols associated with animals in this study were approved by the Medical Ethics Committee of Zunyi Medical University (Approval No.: ZMU21-2412-016), and all methods were carried out in accordance with ARRIVE guidelines and regulations (the anesthesia method used in this study was intramuscular injection of xylazine hydrochloride). The euthanasia method (cervical dislocation performed under deep anesthesia) complied with AVMA guidelines.

2.5.2. Construction of animal models

Bilateral cranial bone defect models were established in all rats. Both defects received the same treatment, and the corresponding scaffolds were implanted in groups. The scaffolds were cylindrical (5 mm in diameter, 1 mm in height), sterilized by irradiation (10 kGy) before implantation, and placed in DMEM complete culture medium overnight for use. SD rats were fasted for 12 h with water deprivation for 8 h before surgery. Anesthesia was induced by intramuscular xylazine hydrochloride. After anesthesia took effect, the skull was prepared, the rats were fixed in a prone position on the operating table, disinfected with 1% povidone-iodine, and draped with sterile sheets. A 2 cm incision was made along the midline at the top of the rat's skull with a scalpel, and the subcutaneous tissue was gently dissected with the handle of the scalpel. Then, the periosteum was neatly incised along the sagittal suture of the skull, and the subperiosteal tissue was carefully dissected with the scalpel handle to fully expose the bilateral parietal bone regions. A 5 mm diameter circular full-thickness bone defect was drilled on both sides of the midline of the rat skull using a hollow burr. After the defect was created, the surgical area was rinsed with an appropriate amount of sterile saline. The scaffolds were then implanted into the skull defects according to the groups, while the blank control group received no scaffolds or materials. After scaffold implantation, the area was rinsed with saline, disinfected with povidone-iodine, and the periosteum and skin were sutured in layers using biodegradable absorbable sutures. Postoperatively, each SD rat was housed individually in a cage and received intramuscular injections of penicillin (800,000 U/day) for three consecutive days.

2.5.3. Blood sampling and specimen collection

At weeks 4, 8, and 12 post-operation, blood was collected from SD rats in each group for testing, and simultaneously, the skull, liver, and kidney tissues were harvested. The skull and implant were completely stripped, excess soft tissue and periosteum were removed, and the complete liver and kidney tissues were collected. The skull specimens and liver and kidney tissues were fixed and preserved in 4% paraformaldehyde for subsequent testing.

The skull specimens fixed with 4% paraformaldehyde were decalcified in EDTA decalcification solution for four weeks, with the decalcification solution changed twice weekly. After decalcification, they were alkalized with 5% sodium sulfate solution, dehydrated with a gradient of ethanol, rinsed with running water, and embedded in paraffin. Continuous coronal sections (5 μm thick) were prepared.

For liver and kidney specimens, after fixation, they were paraffin-embedded, and after embedding was complete, they were sectioned with a microtome (5 μm thick).

2.5.4. Micro-computed tomography

At weeks 4, 8, and 12 post-surgery, the skull specimens from each group were stably placed on the rotating platform of a micro-CT device. The micro-CT device was set with scanning parameters (voltage 80 kV, current 300 μA, copper and aluminum background filtering, exposure time: 340 ms), and the micro-CT was started, with the bone defect as the scanning center. The acquired images were reconstructed, denoised, and enhanced using computer software to obtain 3D images for analysis. Bone repair and ingrowth at the skull defect were observed, and the volume of new bone and tissue at the skull defect was calculated. Statistical analysis was performed on the micro-CT data of different groups of rat skulls to compare differences.

2.5.5. Hematoxylin and eosin staining and Masson staining

For HE staining, after paraffin sectioning, the samples were pre-warmed, placed in xylene (I) for 10 min, xylene (II) for 10 min, and then placed in gradient alcohol for dewaxing. The samples were stained with hematoxylin for 1 min, then rinsed with water to remove excess dye.

They were then placed in 1% hydrochloric acid ethanol for differentiation for 20 s, quickly removed, and immediately placed in running water for blue returning. Water solution containing 1% ammonia was used to continue blue returning for 1 min, followed by dehydration treatment with gradient alcohol. Finally, the slides were mounted with gum sealant, and under an optical microscope, the nuclei appeared dark blue, and the cytoplasm and fibrous tissue appeared red.

For Masson staining, slices were first treated sequentially with environmentally friendly dewaxing solutions I, II, and III, then dehydrated in a gradient of absolute ethanol, and rinsed three times with ultrapure water. Slices stored at −20 °C were equilibrated at room temperature for 30 min, fixed with tissue fixative for 15 min, and then rinsed with flowing deionized water to remove the fixative. Slices were immersed in Masson A solution for nuclear staining, transferred to a mixed stain of Masson B/C for cytoplasmic staining, and sequentially immersed in Masson D, E, and F solutions for collagen color development. After staining, they were differentiated with 1% acetic acid aqueous solution for 10s, dehydrated through a gradient of three levels of absolute ethanol for 3 min each, and finally cleared in xylene for 5 min. Neutral resin was used for mounting. After air drying naturally, images were observed and acquired under an optical microscope.

2.5.6. Immunofluorescence staining

Paraffin sections were dewaxed in xylene (I) and xylene (II) for 10 min each, then placed in gradient alcohol for 2 min each to elute xylene, and rinsed with distilled water. The slices were covered with citrate antigen retrieval solution, and high-pressure cooker treatment technology was used to achieve antigen retrieval. A histochemical pen was used to outline the tissue area, and 3% hydrogen peroxide solution was added to block endogenous peroxidase, incubated at room temperature in the dark for 25 min, and washed with PBS three times, 5 min each. A solution containing 3% BSA was dropped within the histochemical area to evenly cover the tissue, and blocking was performed at room temperature for 30 min. After removing the blocking solution, the sections were incubated with primary antibodies for BMP-2, vascular endothelial growth factor (VEGF), CD163 (M2 macrophage marker), and inducible nitric oxide synthase (iNOS; M1 macrophage marker) at 4 °C overnight. After washing with PBS, they were incubated with corresponding fluorescent secondary antibodies (labeled with Alexa Fluor 488 or 594; bs-1012R, Bioss, China) at room temperature in the dark for 1 h. DAPI was used to counterstain the nuclei. After dehydration and mounting, observation and photography were performed under a fluorescence microscope.

2.6. Statistical analysis

All results in this study were obtained through at least three independent replicates. Data analysis and processing were performed using SPSS 29.0 (IBM Corp., USA). All data are expressed as mean + standard deviation. One-way ANOVA or an independent samples *t*-test was used for comparisons between groups. GraphPad Prism (10.1.2, GraphPad Software, Inc., USA) and Origin software (Origin 2024, OriginLab Corporation, USA) were used for plotting. A p-value < 0.05 was considered statistically significant.

3. Results

3.1. Characterization of ZIF-8

The SEM images in Figure 2A show that the prepared ZIF-8 consists of a large number of discrete particles. Under the microscope, most particles exhibited typical ZIF-8 polyhedral contours, and some particles showed a morphology approximating a rhombic dodecahedron.

To confirm the chemical composition of the sample, EDS area scanning analysis was performed (Figure 2B). The analysis indicated that the sample is primarily composed of four elements: carbon (C), nitrogen (N), zinc (Zn), and a small amount of oxygen (O).

The purity and crystal structure of the sample were analyzed by XRD (Figure 2C). The results showed that the observed diffraction peaks belong to the sodalite topology structure. The diffraction peaks at corresponding positions correspond to the (011), (002), (112), (022), (013), (222), (114), (223), (134) crystal planes of ZIF-8, which are clear markers of successful ZIF-8 formation.

The FTIR spectra shown in Figure 2D demonstrated that FTIR detected vibration peaks caused by the stretching vibration of methyl aliphatic C–H bonds, the stretching vibration of the C=N double bond in the imidazole ring, the stretching vibration of the imidazole ring skeleton, the stretching vibration of the C–N single bond in the imidazole ring, and the out-of-plane bending vibration of C–H in the imidazole ring. These vibration peaks are all characteristic peaks of ZIF-8.

3.2. Characterization of scaffolds

The SEM images (Figure 3A) showed that, compared with the PCL group scaffolds, the surfaces of the LZP and HZP group scaffolds became rougher, and the porosity decreased after ZIF-8 coating. ZIF-8 particles could be seen adhering to the surface.

The EDS analysis (Figure 3B) revealed the elemental composition and content on the surfaces of PCL, LZP, and

HZP scaffolds. No zinc or nitrogen was detected in the PCL scaffold, while zinc and nitrogen were present on the surface of the scaffold after ZIF-8 coating. Furthermore, the zinc and nitrogen content in the HZP scaffold was higher than that in the LZP scaffold.

The porosity of the PCL, LZP, and HZP scaffolds was calculated using the gravimetric method. The porosities of the three groups were (Figure 3C) 77.57 ± 1.38%, 77.71 ± 2.21%, and 76.04 ± 2.32%, respectively. All three groups maintained high porosity levels, and the ZIF-8 coating had a relatively small impact on the porosity of the materials.

The PCL, LZP, and HZP scaffolds were tested using a universal testing machine. The results showed that the compressive strengths of the PCL, LZP, and HZP scaffolds (Figure 3D1) were 14.85 ± 0.75 MPa, 14.98 ± 0.54 MPa, and 14.85 ± 0.63 MPa, respectively, with no statistically significant difference between groups ($p > 0.05$). The compressive moduli were (Figure 3D2) 2,827 ± 31 MPa, 2,967 ± 140 MPa, and 3,036 ± 180 MPa, respectively. There were no significant differences in compressive strength and compressive modulus among the scaffolds ($p > 0.05$), indicating that the ZIF-8 coating had a relatively small impact on the mechanical properties of the scaffolds.

The static contact angles of the three scaffolds were measured using the water droplet method (Figure 3E). The results showed that the PCL scaffold material exhibited stronger hydrophobicity (Figure 3F), with a water contact angle of 85.27 ± 2.80°. The water contact angles of the ZIF-8 modified LZP and HZP scaffolds were 59.99 ± 2.16° and 60.51 ± 4.26°, respectively, which were significantly smaller than those of the PCL scaffold ($p < 0.001$).

The ability of the two groups of ZIF-8-coated scaffolds to release Zn^{2+} was evaluated. The results showed (Figure 3G1) that the concentration of Zn^{2+} released by LZP and HZP scaffolds in PBS solution gradually increased with the number of days, and the concentration of Zn^{2+} released by the HZP group scaffolds was higher than that of the LZP group scaffolds, which is consistent with the trend that the ZIF-8 coating density on the surface of the HZP group scaffolds was higher than that of the LZP group scaffolds (Figure 3G2). The single time point release of Zn^{2+} from LZP and HZP scaffolds in PBS solution showed that the HZP group scaffolds released higher Zn^{2+} than the LZP group scaffolds. By day 14, the daily release concentration of Zn^{2+} from the two groups of scaffolds approached consistency.

The results of FTIR (Figure 3H) showed that the LZP and HZP scaffold groups exhibited vibrational peaks caused by the stretching vibration of the C=N double bond of the imidazole ring near 1,650–1,400 cm^{-1} and out-of-plane bending vibrational peaks of the CH group of the imidazole ring near 750–950 cm^{-1}. This indicates that ZIF-8 was successfully coated on the PCL scaffold surface.

Thermogravimetry-differential scanning calorimetry analysis of the PCL, LZP, and HZP scaffolds showed (Figure 3I) that in the low-temperature region (<250 °C), the thermal stability of the three scaffold materials was similar, with no significant weight loss. Significant thermal weight loss occurred in the range of 300 °C to 450 °C, with mass losses of 99.88%, 99.68%, and 98.98% for the PCL, LZP, and HZP scaffolds, respectively. The mass ratio of the remaining inorganic particles in each scaffold group was close to the density ratio of the ZIF-8 coating.

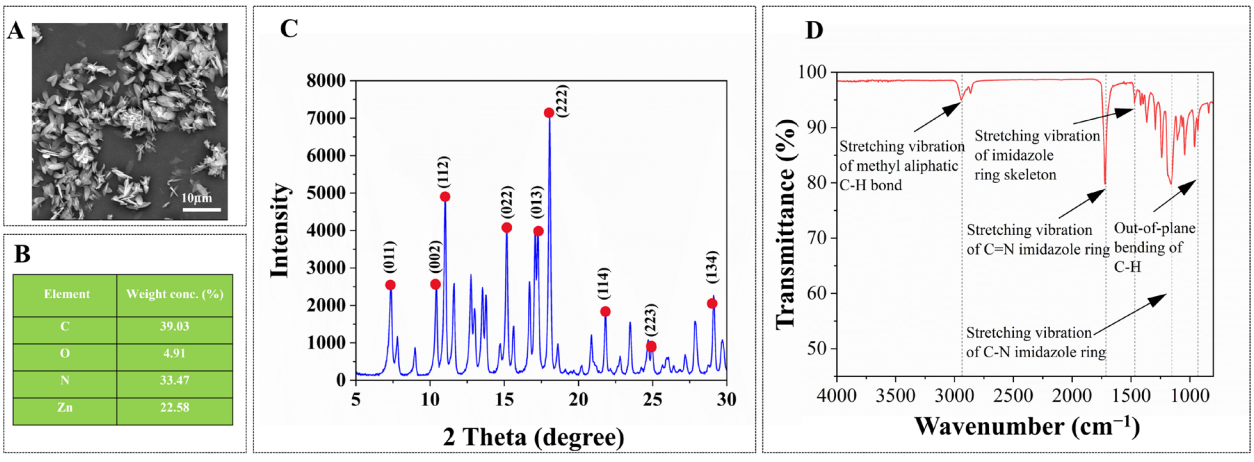

Figure 2. Characterization of the synthesized ZIF-8 particles. (A) Surface morphology of ZIF-8 by scanning electron microscopy. Scale bar = 10 μm; magnification: 5,000×. (B) Elemental composition analysis of ZIF8; (C) XRD of ZIF-8; (D) FTIR spectra of ZIF-8.

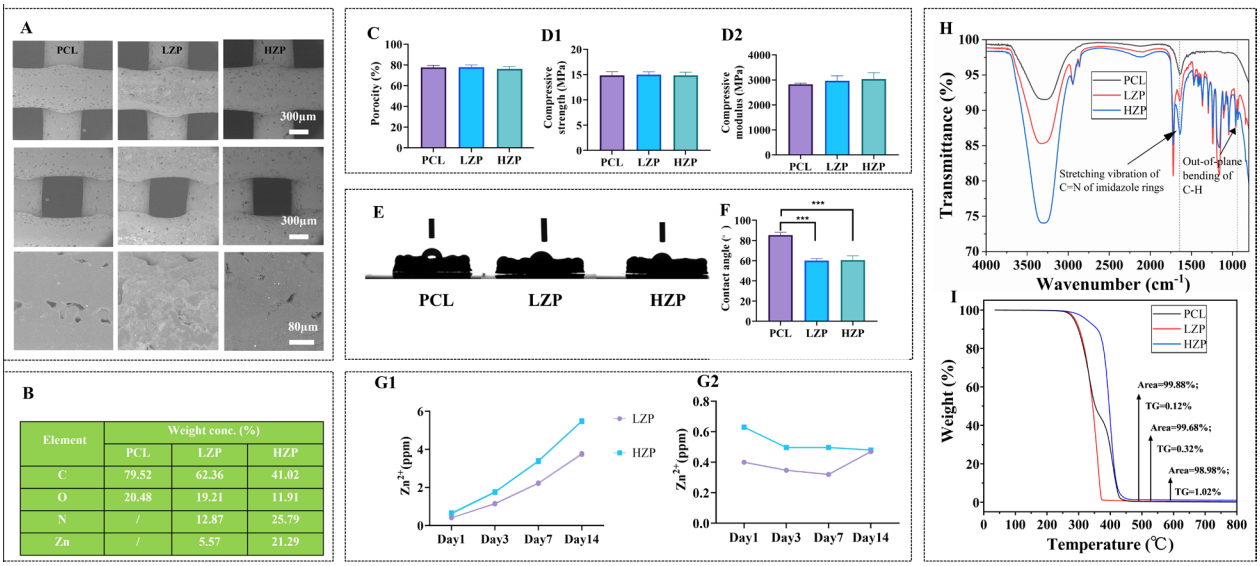

Element	Weight conc. (%)		
	PCL	LZP	HZP
C	79.52	62.36	41.02
O	20.48	19.21	11.91
N	/	12.87	25.79
Zn	/	5.57	21.29

Figure 3. Characterization of polycaprolactone (PCL), low-density ZIF-8-coated PCL (LZP), and high-density ZIF-8-coated PCL (HZP) scaffolds. (A) Surface morphology of PCL, LZP, and HZP scaffolds captured using a scanning electron microscope. Scale bar = 300 μm, 80 μm; magnification: 200×, 1,000×. (B) Elemental composition analysis of PCL, LZP, and HZP scaffolds. (C) Porosity of PCL, LZP, and HZP scaffolds. Mechanical properties of PCL, LZP, and HZP scaffolds: (D1) compressive strength and (D2) compressive modulus. Surface hydrophilicity analysis of PCL, LZP, and HZP scaffolds. (E) Droplet morphology at contact angle. (F) Quantitative analysis of contact angle evaluation (***$p < 0.001$). *In vitro* Zn^{2+} release from LZP and HZP scaffolds: (G1) cumulative release, (G2) single time point release. (H) Fourier transform infrared spectra of PCL, LZP, and HZP scaffolds. (I) Thermogravimetric analysis was used to evaluate the thermal stability and decomposition behavior of PCL, LZP, and HZP scaffolds.

3.3. Effect of scaffolds on the proliferation capacity of bone marrow mesenchymal stem cells

Bone marrow mesenchymal stem cells were cultured on the scaffold surface, and cell proliferation was observed after 1, 3, and 7 days of culture. The results (Figure 4A) showed that after 1 day of culture, there was no significant difference in BMSC cell proliferation among the three scaffold groups ($p > 0.05$). After 3 days of co-culture, the LZP and HZP groups showed significantly higher BMSC cell proliferation than the PCL group ($p < 0.0001$). However, after 7 days of co-culture, the number of proliferating BMSCs in the LZP group was significantly higher than that in the PCL and HZP groups, and the proliferation of BMSCs in the HZP group was significantly lower than that in the PCL group; all comparisons between groups were statistically significant ($p < 0.0001$). The viability of BMSCs on the three scaffolds was assessed using live/dead cell fluorescence staining. Cell viability was observed after 3 days of co-culture with the scaffolds. The results (Figure 4B) showed that the LZP group had significantly more BMSCs adhering to it than the PCL and HZP groups, and the green fluorescence signal was significantly enhanced and more uniformly distributed.

3.4. Direct osteogenic capacity of the scaffolds

The ability of the three scaffolds to promote early direct osteogenic differentiation was assessed by ALP staining and quantitative activity analysis. Results (Figure 5A and 5B) showed that the intensity and quantification of direct osteogenic ALP staining in the LZP group on day 7 were higher than those in the PCL and HZP groups. The ability of the three scaffolds to promote late-stage direct osteogenic differentiation was assessed by Alizarin Red staining and quantitative analysis. Results (Figure 5C and 5D) showed that the intensity and quantification of direct osteogenic Alizarin Red staining in the LZP group on day 7 were higher than those in the PCL and HZP groups. RT-qPCR was used to detect differences in osteogenesis-related gene expression among the three scaffolds on days 7 and 14 after direct osteogenic induction. Results (Figure 5E) showed that the expression of *Bmp2*, *Col1a1*, *Alpl*, and *Runx2* genes in the LZP group on days 7 and 14 after direct osteogenic induction was significantly higher than that in the PCL and HZP groups ($p < 0.05$).

3.5. Immunomodulatory capacity of the scaffold

The expression of macrophage polarization-related cytokines and genes in macrophages at 1 and 3 days after induction using ELISA and RT-qPCR experiments in the three scaffold groups was detected. The results (Figure 6A) showed that, compared with PCL and HZP, the LZP group upregulated the expression of the M2 macrophage-

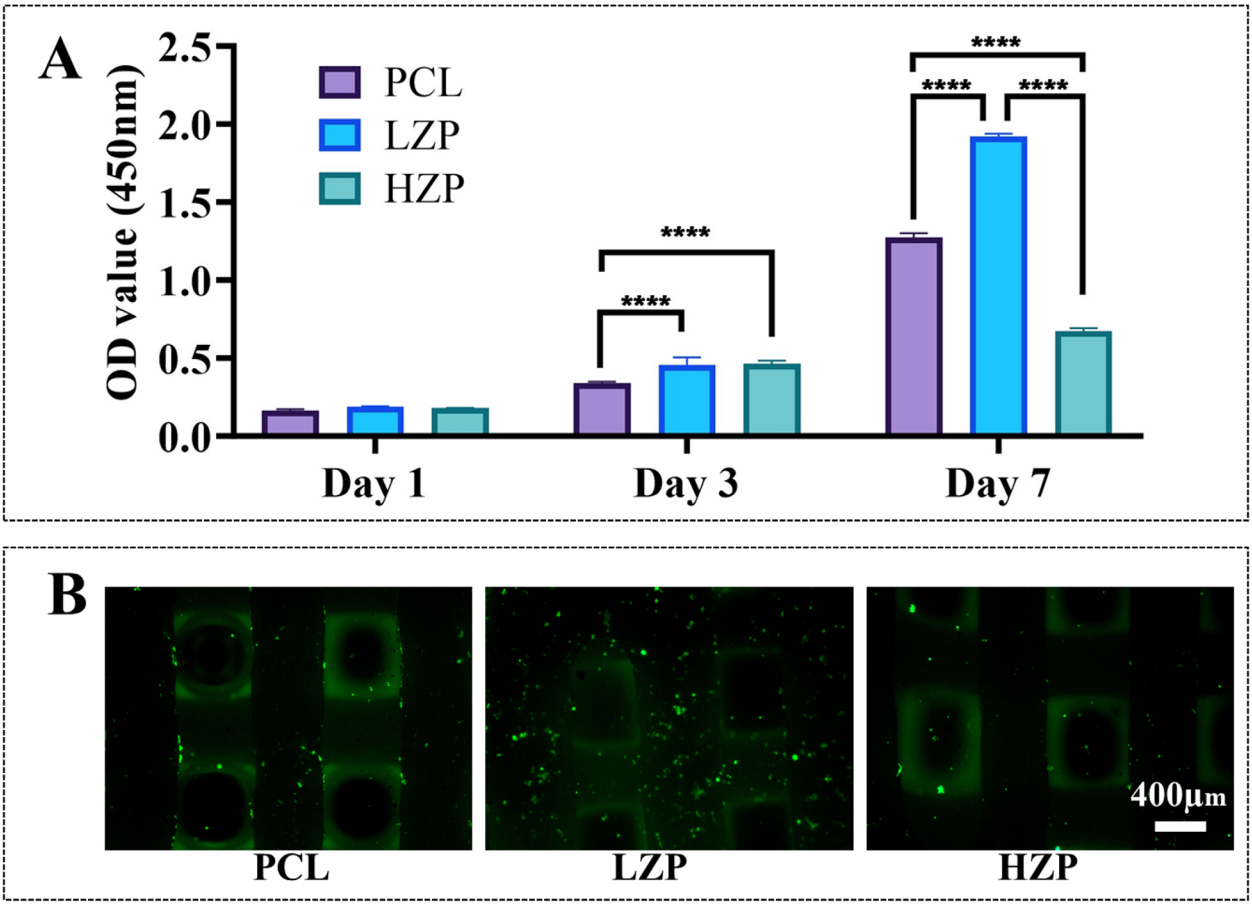

Figure 4. Biocompatibility and cell proliferation of bone marrow mesenchymal stem cells (BMSCs) on different scaffolds. (A) CCK-8 assay to detect BMSC proliferation after culturing with polycaprolactone (PCL), low-density ZIF-8-coated PCL (LZP), and high-density ZIF-8-coated PCL (HZP) scaffolds for 1, 3, and 7 days, respectively (****$p < 0.0001$) ;(B) Live cell fluorescence staining on the surface of scaffolds after co-culturing BMSCs with PCL, LZP, and HZP scaffolds for three days (scale bar = 500 μm; magnification: 5×).

related cytokine IL-10 and inhibited the expression of the M1 macrophage-related cytokine IL-12. The LZP group upregulated the expression of M2 macrophage-related genes (*Cd206* and *Arg1*) and inhibited the expression of M1 macrophage-related genes (*Tnfa* and *Il1b*). The differences in osteogenesis-related gene expression among the three scaffold groups at 1 and 3 days after immunomodulatory osteogenic induction were detected by RT-qPCR. The results (Figure 6B) showed that the expression of *Arg1*, *Tnfa*, *Il1b*, and *Cd206* genes in the LZP group was significantly higher than that in the PCL and HZP groups at 7 and 14 days after immunomodulatory osteogenic induction ($p < 0.05$).

3.6. Osteogenic capacity of the scaffolds

After three days of culture with the respective scaffold groups, the supernatants from RAW264.7 cells were collected. Macrophage-conditioned osteogenic medium for each group was prepared by mixing the supernatants with osteogenic induction medium at a 1:1 volume ratio. To mimic the immunomodulatory microenvironment, BMSCs were cultured with the scaffolds using the corresponding macrophage-conditioned osteogenic medium. This setup was used to evaluate the ability of each scaffold group to regulate M2 phenotype polarization to promote the osteogenic differentiation of BMSCs. The ability of the three scaffolds to promote early immune-regulated osteogenic formation was assessed by ALP staining and activity quantification. The results (Figure 7A and 7B) showed that the ALP staining intensity and quantification in the LZP group on day 7 were higher than those in the PCL and HZP groups. The ability of the three scaffolds to promote late-stage immune-regulated osteogenic formation was assessed by Alizarin Red staining and quantification. The results (Figure 7C and 7D) showed that the Alizarin Red S

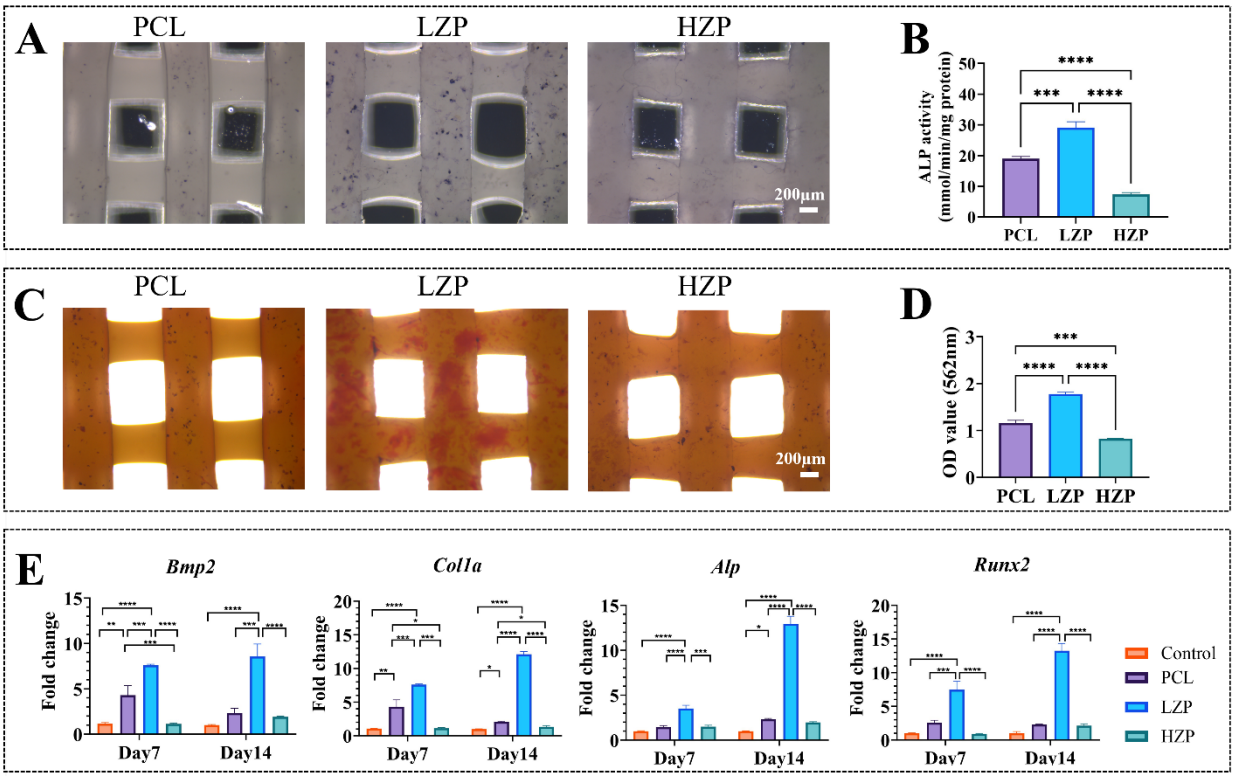

Figure 5. Direct osteogenic differentiation of bone marrow mesenchymal stem cells (BMSCs) induced by different scaffolds. (A) Alkaline phosphatase (ALP) staining image of BMSCs cultured on scaffolds for seven days (scale bar: 200 μm; magnification: 5×). (B) Quantitative analysis of direct osteogenic ALP activity. (C) Alizarin Red S staining image of BMSCs cultured on scaffolds for 14 days(scale bar: 200μm; magnification: 5×). (D) Quantitative analysis of direct osteogenic Alizarin Red S activity. (E) Expression of osteogenesis-related genes after direct osteogenic induction of BMSCs with polycaprolactone (PCL), low-density ZIF-8-coated PCL (LZP), and high-density ZIF-8-coated PCL (HZP) scaffolds for 7 and 14 days (* indicates $p < 0.05$, ** indicates $p < 0.01$, *** indicates $p < 0.001$, **** indicates $p < 0.0001$)

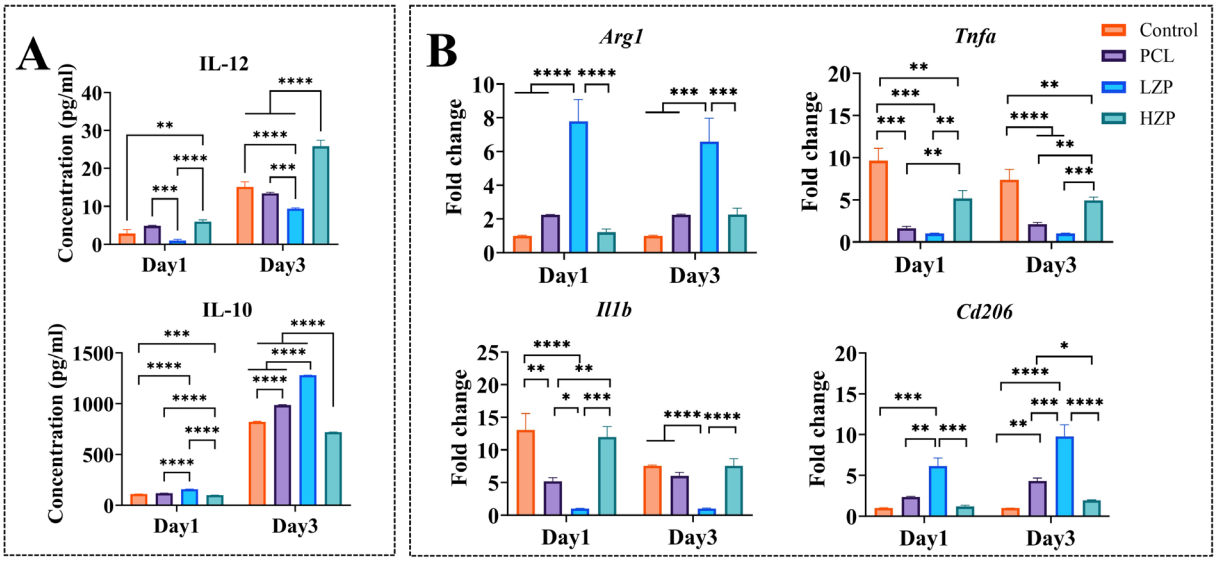

Figure 6. Immunomodulatory effects of different scaffolds on macrophage polarization. (A) ELISA analysis of macrophage polarization-related cytokine levels after RAW264.7 cells were cultured on polycaprolactone (PCL), low-density ZIF-8-coated PCL (LZP), and high-density ZIF-8-coated PCL (HZP) scaffolds for 1 and 3 days. (B) Expression of macrophage polarization-related genes after RAW264.7 cells were cultured on PCL, LZP, and HZP scaffolds for 1 and 3 days.

staining intensity and quantification in the LZP group on day 14 were higher than those in the PCL and HZP groups. RT-qPCR was used to detect differences in osteogenesis-related gene expression among the three scaffolds on days 7 and 14 after immune-regulated osteogenic induction. Results (Figure 7E) showed that the expression of *Bmp2*, *Col1a1*, *Alpl*, and *Runx2* genes in the LZP group on days 7 and 14 after immune-regulated osteogenic induction was significantly higher than that in the PCL and HZP groups ($p < 0.05$).

3.7. *In vivo* osteogenic capacity of the scaffolds

3.7.1. Micro-computed tomography

To evaluate the bone repair efficacy of the three scaffolds *in vivo*, we monitored the bone repair process of SD rats with cranial defects implanted with scaffolds at 4, 8, and 12 weeks using micro-CT. The results (Figure 8A) showed that the amount of new bone formation in the unscaffolded control group was low. The PCL, LZP, and HZP groups showed significantly increased new bone tissue compared to the control group. At 4 and 8 weeks post-operation, the amount of new bone formation in the bone defect area of the control group was low, and at 12 weeks, there was still no significant increase in new bone tissue, indicating poor bone repair without scaffold implantation. At 4 weeks post-operation, the PCL and HZP groups showed low new bone formation. In the subsequent 8 and 12 weeks, new bone tissue increased, but large bone defects were still observed, demonstrating that the bone repair capacity of the PCL and HZP scaffolds was limited. In contrast, the LZP group showed greater new bone formation at all time points, with a significant increase in trabeculae and lamellar bone at 12 weeks, indicating that the LZP scaffold effectively accelerated the bone defect repair process. Quantitative analysis was performed on the bone volume

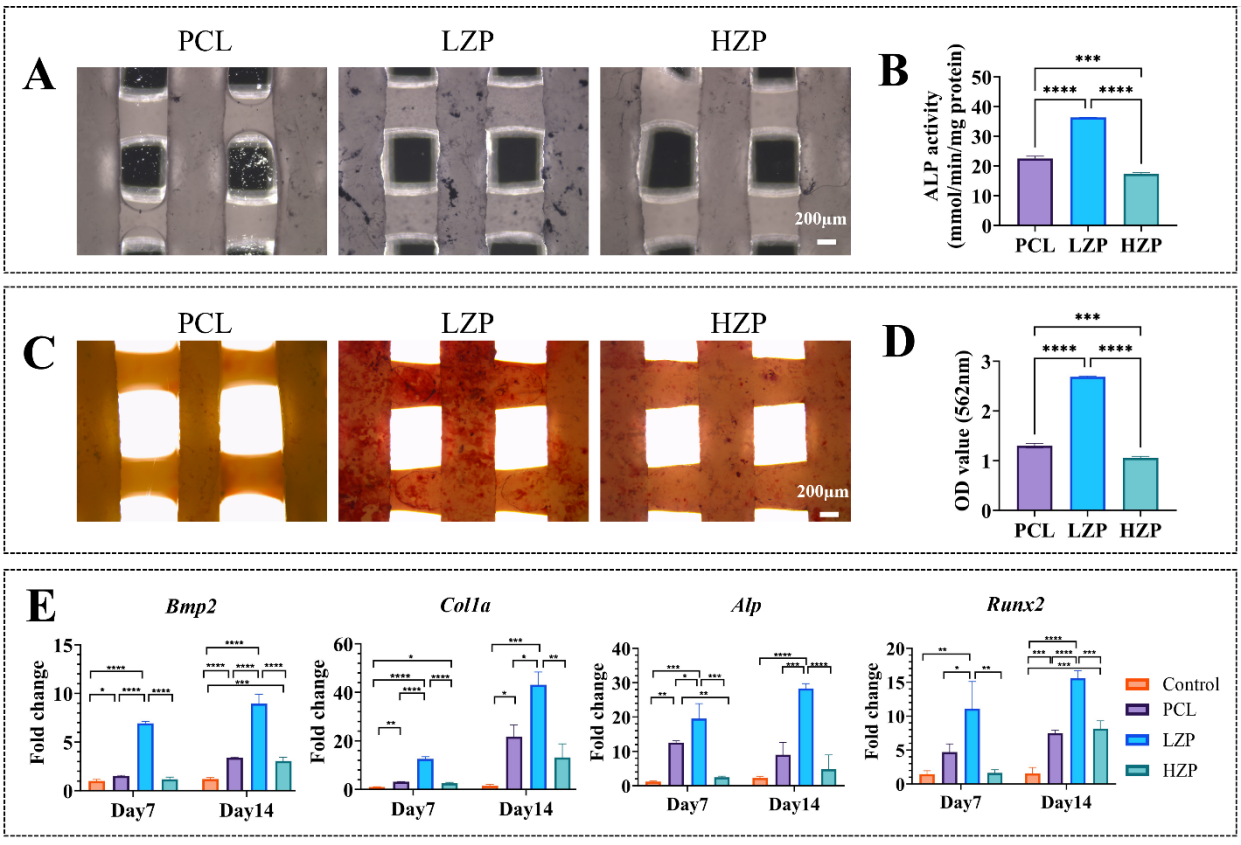

Figure 7. Osteogenic differentiation of bone marrow mesenchymal stem cells (BMSCs) under macrophage-mediated immunomodulation. (A) Alkaline phosphatase (ALP) staining of BMSCs cultured on scaffolds for 7 days (scale bar: 200μm; magnification: 5×). (B) Quantitative analysis of ALP activity in immunomodulatory osteogenic processes. (C) Alizarin Red S staining image of BMSCs cultured on scaffolds for 14 days (scale bar: 200μm; magnification: 5×). (D) Quantitative analysis of Alizarin Red S staining. (E) Expression of osteogenesis-related genes in BMSCs cultured on polycaprolactone (PCL), low-density ZIF-8-coated PCL (LZP), and high-density ZIF-8-coated PCL (HZP) scaffolds after 7 and 14 days of immunomodulatory osteogenic induction (* indicates $p < 0.05$, ** indicates $p < 0.01$, *** indicates $p < 0.001$, **** indicates $p < 0.0001$).

fraction (BV/TV [%]) and bone mineral density (BMD) of different groups at 4, 8, and 12 weeks after surgery (Figure 8B). The bone repair effect of the LZP scaffold was the most significant ($p < 0.05$), and these differences were statistically significant.

3.7.2. Hematoxylin and eosin and Masson staining

To further validate the bone defect repair effects of the three scaffolds *in vivo*, we collected rat skull specimens at weeks 4, 8, and 12 post-surgery. HE staining and Masson staining were used to analyze the newly formed bone tissue at the bone defect site. As shown in Figure 9A, at week 4, the defect area in the control group was mainly composed of fibrous tissue. In the PCL and HZP groups, a small amount of new bone began to appear in the defect area. In contrast, the LZP group showed a more obvious area of new bone formation, with the new bone tissue gradually darkening in color and being more widely distributed. New bone tissue gradually formed in the pores of the scaffold, and was observed at the defect interface and inside the material. At weeks 8 and 12, compared with the other two groups, the LZP group showed a significantly larger area of new bone formation, a significantly smaller bone defect area, and the formation of continuous trabecular bone structures. As shown in Figure 9B, the new bone tissue in each group further matured over time, with the dark blue collagen gradually maturing. At week 4, the LZP group showed more light blue collagen tissue. At 8 and 12 weeks, the collagen fiber maturity in the LZP group was significantly improved, showing dense, regularly arranged blue staining areas, and mature new bone had formed and grown into the scaffold. The limited tissue infiltration observed within scaffold pores in histological sections may be attributed to sectioning orientation and tissue loss during preparation, as confirmed by micro-CT analysis.

3.7.3. Immunohistochemical fluorescent Staining

To further investigate the scaffold's immunomodulatory,

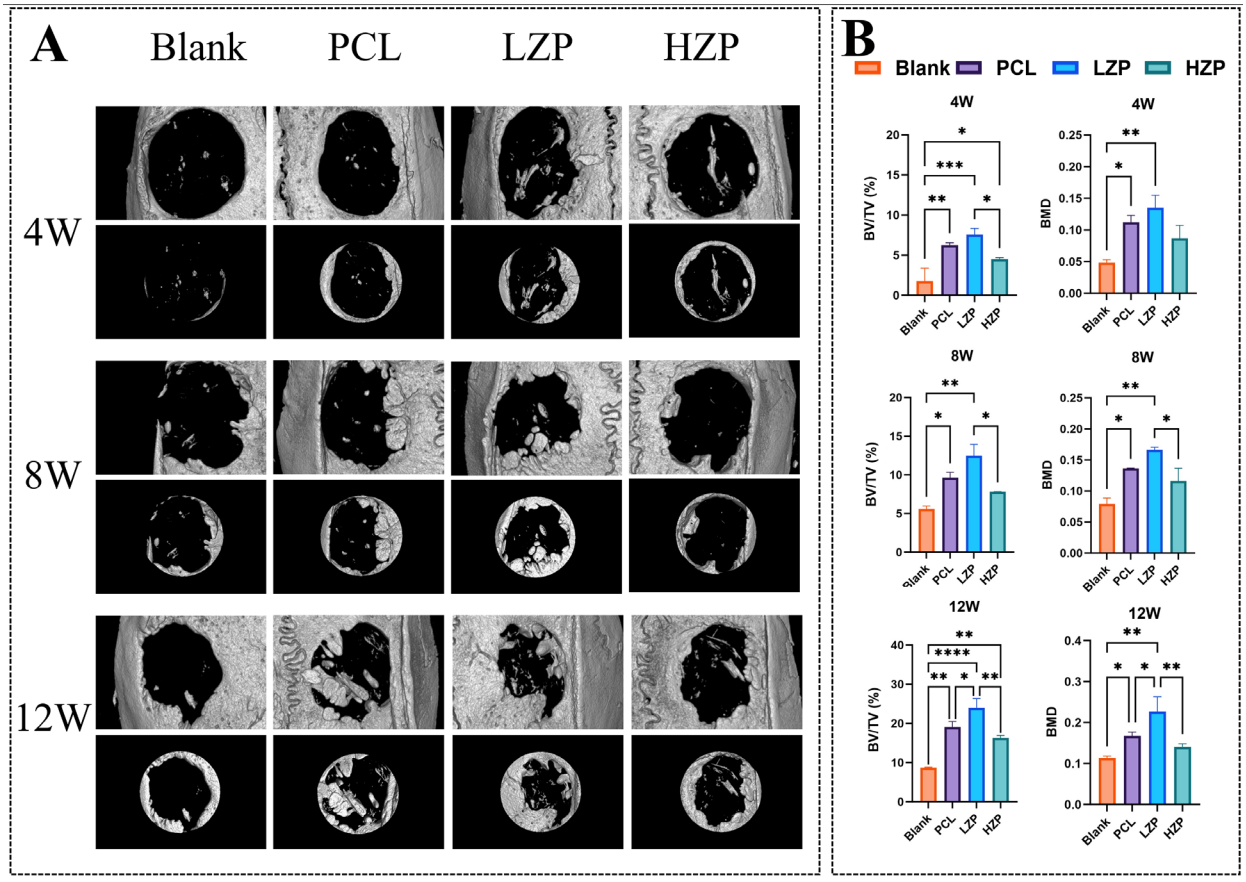

Figure 8. Micro-computed tomography transverse images of skull defects in rats at 4, 8, and 12 weeks post-surgery, analysis of bone volume fraction (BV/TV [%]) and bone mineral density (BMD) at the bone defect site. (* indicates $p < 0.05$, ** indicates $p < 0.01$, *** indicates $p < 0.001$, **** indicates $p < 0.0001$).
Abbreviations: HZP: High-density ZIF-8-coated PCL; LZP: Low-density ZIF-8-coated PCL; PCL: Polycaprolactone.

angiogenesis-promoting, and osteogenic differentiation capabilities, immunofluorescence staining was used to detect iNOS (red), CD163 (green), VEGF (red), and BMP-2 (green) in the bone defect areas of each group. The results (Figure 10A and 10B) showed that, in terms of immune regulation, iNOS and CD163 were polarization markers of macrophage M1 and M2 types, respectively. At 4, 8, and 12 weeks post-surgery, the color of the red fluorescent expression area (iNOS) gradually decreased. The blank group showed stronger red fluorescence (iNOS) expression in the newly formed tissue of the bone defect area, while at week 12, the LZP group scaffold showed weaker red fluorescence compared to other groups. At 4, 8, and 12 weeks post-surgery, the color of the green fluorescent expression area (CD163) gradually increased, with a stronger green fluorescent area observed in the LZP group at week 12. The fluorescence results of iNOS and CD163 indicate that the LZP scaffold can promote the expression of macrophage M2 type and inhibit the expression of macrophage M1 type, thus exerting a better immune regulatory effect and facilitating bone defect repair. Regarding angiogenesis, at 4, 8, and 12 weeks post-surgery, the red fluorescence (VEGF) in the bone defect area of each scaffold gradually increased. At week 12, the LZP group scaffold showed stronger red fluorescence over a wider area, indicating that the LZP group scaffold could better promote angiogenesis in the bone defect area, which is beneficial for bone defect repair. Regarding osteogenic differentiation, the green fluorescence (BMP-2) of each scaffold gradually increased at 4, 8, and 12 weeks post-surgery. At week 12, the LZP group scaffold showed stronger green fluorescence expression.

3.8. Biocompatibility of scaffolds

3.8.1. Blood indicator detection

At weeks 4, 8, and 12 post-surgery, there were no statistically significant differences in routine blood parameters, white blood cell, red blood cell, hemoglobin, platelet, alanine aminotransferase, aspartate aminotransferase, creatinine, and urea in the blank group, PCL, LZP, and HZP groups ($P > 0.05$).

3.8.2. Hematoxylin and eosin staining of liver and kidney tissues

To assess the biocompatibility of the scaffold, the liver and kidneys of rats in each group were removed at 4, 8, and 12 weeks post-surgery, and pathological tissue sections were prepared. HE staining was used to analyze whether

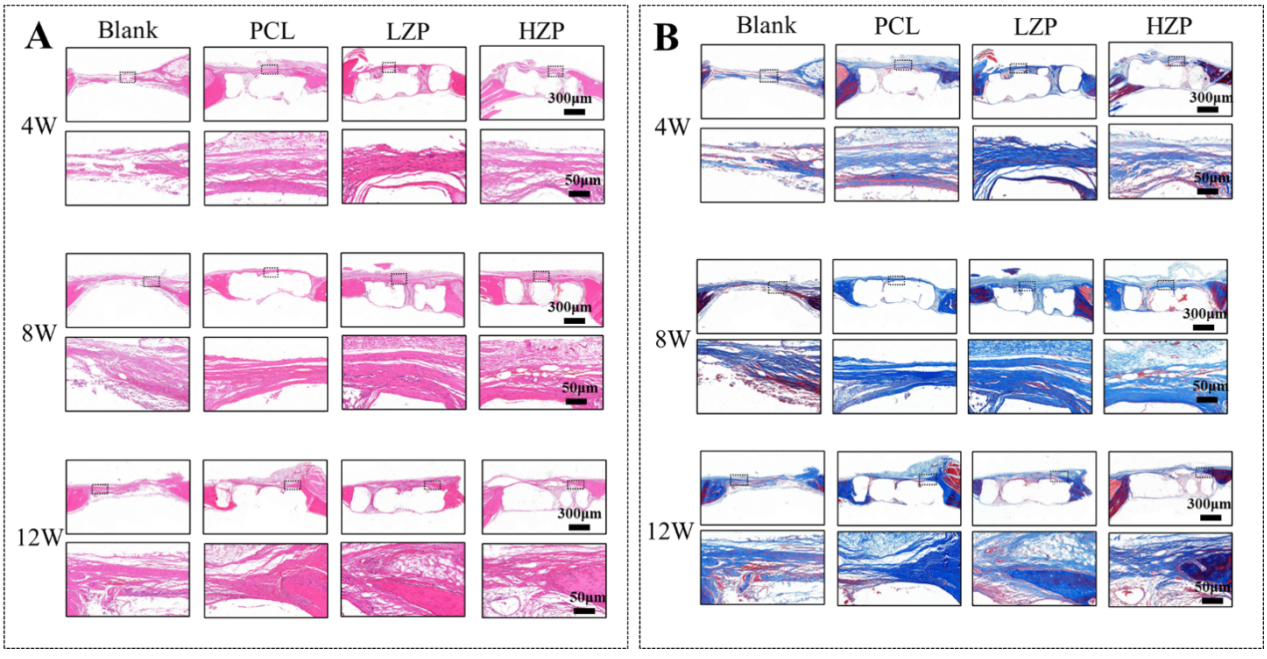

Figure 9. Histological evaluation of new bone formation by hematoxylin and eosin (HE) and Masson staining. (A) HE staining of rat skulls at 4, 8, and 12 weeks post-surgery (scale bar 300 μm, 50 μm; magnification: 3×, 20×). (B) Masson staining of rat skulls at 4, 8, and 12 weeks post-surgery (scale bar 300 μm, 50 μm; magnification: 3×, 20×).
Abbreviations: HZP: High-density ZIF-8-coated PCL; LZP: Low-density ZIF-8-coated PCL; PCL: Polycaprolactone.

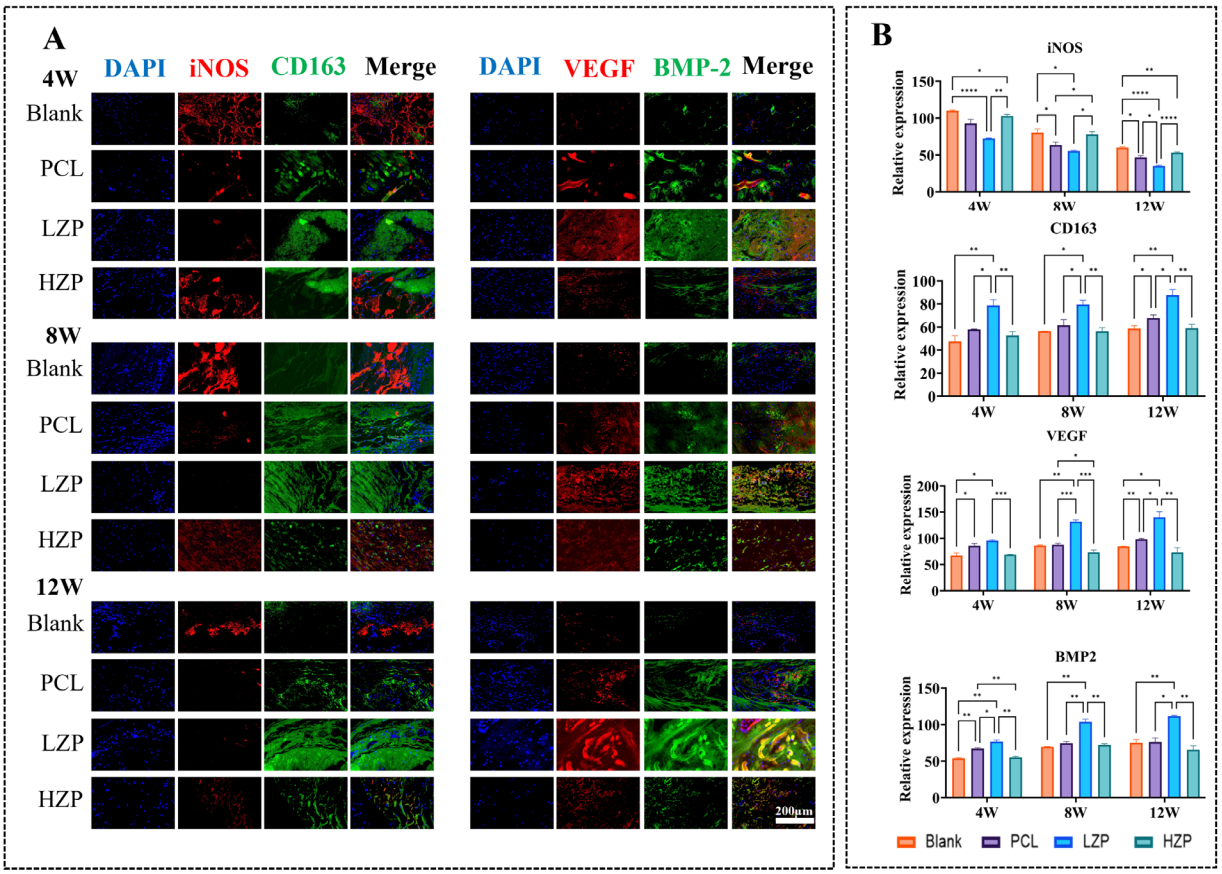

Figure 10. Immunofluorescence analysis of immune modulation, angiogenesis, and osteogenesis at the cranial defect. (A) Expression of iNOS, CD163, VEGF, and BMP-2 in the bone defect area of rats in each group at 4, 8, and 12 weeks after surgery. (Scale bar: 200 μm; magnification: 30×). (B) Quantitative analysis of the fluorescence intensity of inducible nitric oxide synthase (iNOS), CD163, vascular endothelial growth factor (VEGF), and bone morphogenetic protein 2 (BMP-2) in each group.
Abbreviations: HZP: High-density ZIF-8-coated PCL; LZP: Low-density ZIF-8-coated PCL; PCL: Polycaprolactone.

lesions occurred. As shown in Figure 11A and 11B, specific structures such as central veins, portal areas, hepatocytes, glomeruli, renal tubules, and mesangial cells were clearly visible in the liver and kidney tissues of rats in each group. The morphology and boundaries were normal, and no inflammatory cell infiltration was observed, indicating that the scaffold material in each group was not hepatotoxic or nephrotoxic.

4. Discussion

Ideal bone repair materials should possess biocompatibility and biodegradability, while also exhibiting osteoconductivity, mechanical strength, and the ability to effectively induce new bone formation.[28] This study addressed the issues of high hydrophobicity and poor cell adhesion in 3D-printed PCL scaffolds by modifying their surface with ZIF-8 of different densities. The performance differences between LZP and HZP scaffolds were systematically investigated. The results showed that the ZIF-8-coated PCL scaffolds maintained good porosity and mechanical strength while improving hydrophilicity. The LZP scaffolds exhibited better biocompatibility and bone differentiation promotion capacity compared to both PCL and HZP scaffolds. Furthermore, the study found that the LZP scaffolds correlated with macrophage polarization towards the M2 phenotype, improving the local immune microenvironment. In a rat skull defect model, the LZP scaffolds significantly promoted bone regeneration.

Traditional PCL coatings often utilize inorganic minerals such as hydroxyapatite or other polymers such as polylactic acid to apply a single coating to the surface of PCL materials. Although this can promote cell adhesion and proliferation, the functional integration is low, making it difficult to simultaneously achieve osteoinduction, antibacterial properties, and controlled drug release. Furthermore, it relies heavily on exogenous biomolecules

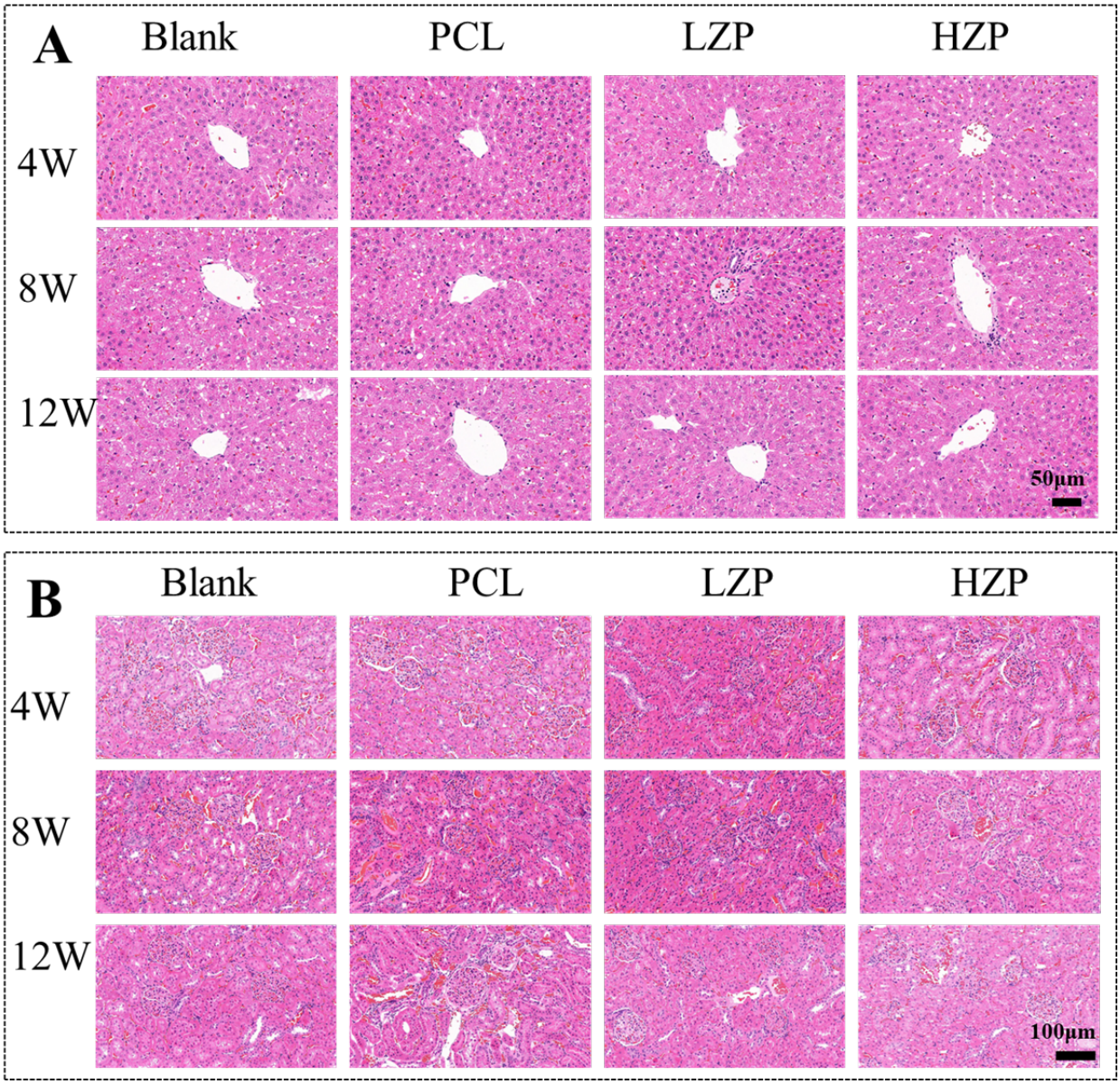

Figure 11. *In vivo* biocompatibility assessment of scaffolds in liver and kidney tissues. (A) HE staining of rat livers at 4, 8, and 12 weeks post-surgery (scale bar: 50 μm; magnification: 36×). (B) Hematoxylin and eosin staining of rat kidneys at 4, 8, and 12 weeks post-surgery (scale bar: 100 μm; magnification: 22×).

Abbreviations: HZP: High-density ZIF-8-coated PCL; LZP: Low-density ZIF-8-coated PCL; PCL: Polycaprolactone.

for promoting bone activity.[29] ZIF-8-coated PCL scaffolds, on the other hand, can serve as a multifunctional active platform. Leveraging its Zn^{2+}-controlled release capability, high loading capacity, pH-responsive release, and antibacterial and osteogenic properties, it synergistically promotes bone regeneration to address more complex bone defect problems. In previous studies, some researchers have directly incorporated ZIF-8 into PCL scaffolds to enhance osteogenic efficacy, such as Zhong *et al.*[30] ZIF-8 was combined with PCL and calcium dihydrogen phosphate dihydrate to prepare a 3D-printed composite scaffold. Results showed that ZIF-8 significantly enhanced the scaffold's osteogenic and antibacterial properties. Furthermore, Chen *et al.*[21] coated ZIF-8 particles onto the surface of multi-control titanium, and the experimental results showed that the ZIF-8 coating could enhance the osteogenic activity of titanium materials. These studies confirm the application potential of ZIF-8 and its coating

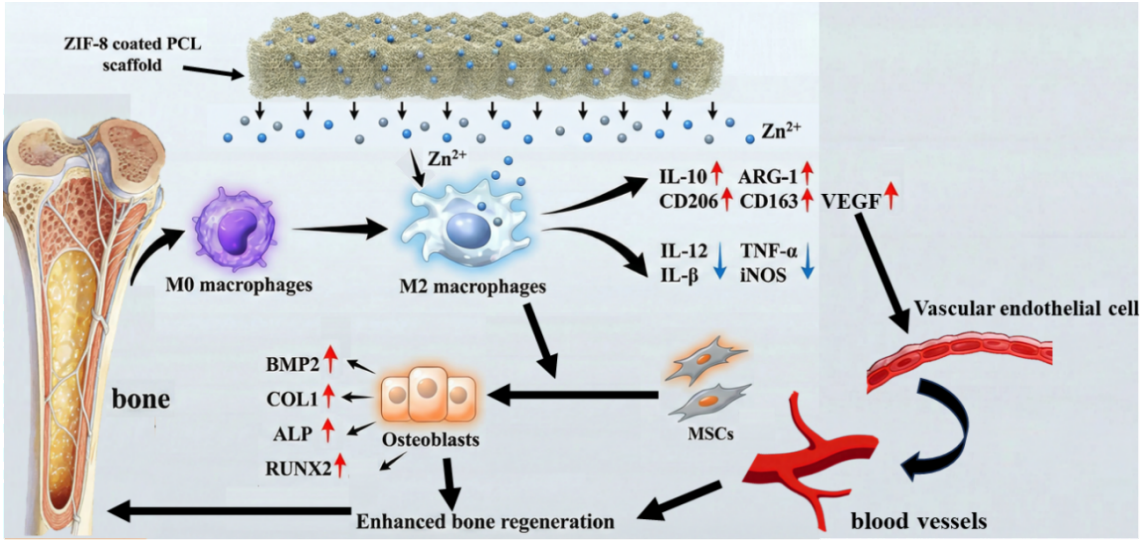

Figure 12. Schematic diagram of the immune regulation mechanism of osteogenic ZIF-8-coated PCL scaffold
Abbreviations: ALP: Alkaline phosphatase; ARG-1: Arginase-1; BMP2: Bone morphogenetic protein 2; CD163: Hemoglobin scavenger receptor; CD206: Differentiation cluster 206 (mannose receptor); COL1: Type I collagen; IL-10: Interleukin-10; IL-12: Interleukin-12; IL-1β: Interleukin-1β; iNOS: Inducible nitric oxide synthase; M0: Monocyte-derived macrophages; M2: Replacement activated macrophages; MSCs, mesenchymal stem cells; PCL, polycaprolactone; RUNX2: Runt-related transcription factor 2; TNF-α: Tumor necrosis factor-α; VEGF: Vascular endothelial growth factor; ZIF-8: Zeolite imidazolate framework-8.

material in promoting bone growth.

Although previous studies have validated the potential of ZIF-8 in bone repair, systematic research on the effects of coating configuration parameters on Zn^{2+} release behavior and its bone immune regulation effect remains limited. Therefore, this study systematically evaluated the Zn^{2+} release characteristics, immune polarization behavior, and osteogenic repair effects of ZIF-8-coated PCL scaffolds with different densities by constructing them, and explored that their concentration may contribute to induced M2 polarization and thereby promote osteogenesis. First, this study used 3D printing to prepare PCL scaffolds. Then, using a solution stirring method, the PCL scaffolds were modified with ZIF-8 of different densities to prepare LZP and HZP. SEM observation of the morphological characteristics of the PCL, LZP, and HZP scaffolds revealed that the LZP and HZP scaffolds had a rougher surface after coating, with particles visible under high magnification, likely due to the adhesion of the ZIF-8 coating (Figure 3A). This indicates that the addition of ZIF-8 increases the surface roughness of the scaffolds, which is more conducive to cell adhesion. Furthermore, studies have confirmed that the porous structure and metallic nodes (Zn^{2+}) of ZIF-8 help enhance the surface energy of the material, thereby increasing its attraction to water molecules and improving its hydrophilicity.[31] The LZP and HZP scaffolds prepared in this study exhibited better hydrophilicity after the ZIF-8 coating (Figure 3E), providing more favorable conditions for cell adhesion and proliferation. Meanwhile, Fourier transform infrared spectroscopy revealed characteristic absorption peaks of ZIF-8 in the LZP and HZP groups near 1,650–1,400 cm^{-1} and 750–950 cm^{-1} (Figure 3H). These peaks are attributed to the stretching vibration of the C=N double bond in the imidazole ring and the out-of-plane bending of the CH group in the imidazole ring, respectively, indicating that ZIF-8 was successfully coated onto the PCL material surface.[32] In this study, the porosity of the PCL, LZP, and HZP scaffolds remained at a high level, and there was no significant difference in porosity among the scaffolds (Figure 3C), confirming that the introduction of the ZIF-8 coating did not change the pore structure of the scaffolds. This high porosity is beneficial to cell adhesion and blood vessel growth. In terms of mechanical properties, the compressive strength and compressive modulus of the PCL, LZP, and HZP scaffolds did not differ significantly, and all maintained a high level capable of withstanding certain mechanical loads (Figure 3D), indicating that the ZIF-8 coating had little impact on the mechanical properties of the scaffolds. Thermogravimetric analysis was used to evaluate the thermal stability of the scaffolds. The results showed that the mass of the remaining inorganic particles in the LZP and HZP scaffolds was close to the theoretical ratio of the ZIF-8 density when coated (Figure 3I), and all three scaffolds exhibited good thermal stability. Finally, the ion release capacity of the scaffolds was

evaluated through *in vitro* ion release experiments (Figure 3G). Both coated scaffolds were able to stably release Zn^{2+}, and the concentration of Zn^{2+} released by the HZP scaffold was consistently higher than that of the LZP scaffold.

The biosafety of bone repair materials is fundamental to their clinical translation and directly relates to patient safety and treatment prognosis. Bone repair materials implanted in the body interact with the host's immune system, blood system, and surrounding tissues. Materials lacking biocompatibility can trigger a series of harmful reactions, potentially leading to implantation failure, infection, inflammation, or even rejection by the host.[33,34] Therefore, the biocompatibility of bone repair materials must first be analyzed, including cytotoxicity, blood compatibility, and assessment of vital organs. To test the biocompatibility of the scaffolds, BMSCs were seeded on three groups of scaffolds: PCL, LZP, and HZP. The growth of cells on the scaffold surface was then observed by live/dead cell staining. The results showed that none of the three groups of scaffolds had significant cytotoxicity, and the LZP group of scaffolds significantly promoted the proliferation of BMSCs. At the same time, the proliferation of BMSCs on each group of scaffolds was detected by the CCK-8 assay after 1, 3, and 7 days of culture (Figure 4A). The results showed that the LZP group of scaffolds had the strongest cell proliferation-promoting ability, and the difference was statistically significant ($p < 0.0001$), indicating that the scaffold with low-density ZIF-8 coating is more conducive to cell adhesion and proliferation. Since the degradation products of the implanted materials themselves and the substances produced by their interaction with the body's microenvironment may relatively reduce biological performance, surface roughness and hydrophilicity are two major factors affecting the biocompatibility of materials. Surface roughness affects the actual surface area of a material. Moderate surface roughness increases the actual surface area, providing more attachment points for cell pseudopodia and thus enhancing cell adhesion.[35] Hydrophilicity reflects the material's surface affinity for water. Hydrophilic surfaces are usually represented by a low water contact angle, allowing for more effective adsorption of adhesion-promoting proteins in cell culture medium or serum, facilitating recognition and binding by adhesion receptors on the cell membrane.[36] Studies have shown that high concentrations of ZIF-8 particles may impair early cell responses. For example, Johari *et al.*[26] showed that when the ZIF-8 exposure concentration increased from 0 to 500 μg/mL, the viability of human embryonic kidney cells (HEK293) was significantly reduced, with a 24-h half-maximal inhibitory concentration of 116.22 μg/mL. Therefore, to further clarify the biocompatibility of the materials, this study established an SD rat animal model and extracted peripheral blood indicators for testing according to groups (Table 1). Liver and kidney tissues were also collected for HE staining (Figure 11). The results showed that the peripheral blood results of the PCL, LZP, and HZP groups were all within the normal range, and the differences were not statistically significant ($p > 0.05$). HE staining of liver and kidney tissues in each group showed no obvious lesions, indicating that the coated scaffolds were not cytotoxic.

Alkaline phosphatase is a classic marker of early osteoblast differentiation, while calcium nodule deposition is a marker of late-stage osteoblast functional maturity and evidence of bone formation. Both can be used to assess the ability of bone repair materials to promote bone differentiation and bone formation.[37,38] To detect the direct osteogenic properties of the PCL, LZP, and HZP scaffolds, we used ALP staining, Alizarin Red staining, and quantitative detection of changes in these two markers (Figure 5) to further confirm that the low-density ZIF-8 coating can enhance the osteogenic capacity of PCL. Osteogenic differentiation of stem cells is a complex process involving the synergistic effects of multiple genes, transcription factors, signaling pathways, and cytokines. Regarding osteogenic gene expression, *BMP2* is the initial signal initiating osteogenic differentiation. BMP-2 activates a series of signaling pathways, inducing and regulating the expression of downstream osteogenesis-related genes, thereby promoting the differentiation of mesenchymal stem cells into osteoblasts.[39] RUNX2 is a transcription factor downstream of the BMP signaling pathway and a master regulator in osteoblast differentiation and bone formation. It is considered one of the earliest markers of osteogenic differentiation, and its expression and activity continue throughout the entire process of osteoblast differentiation and maturation.[40] ALP is a key early marker of osteoblastogenesis. It is a typical protein product of osteoblast phenotype and differentiation, and changes in its gene expression level can reflect the state of osteogenic activity.[41] Col-I is the main organic component of the extracellular matrix of osteoblasts, playing an important role in the formation and structural integrity of the cell's organic matrix. It can stimulate osteoblast adhesion and differentiation and is key to bone tissue mineralization.[42] Studies have shown that Zn^{2+} can effectively promote osteogenic differentiation at appropriate concentrations. For example, 50 μM Zn^{2+} has been shown to effectively increase the ALP activity and osteogenesis-related gene expression levels in mouse BMSCs.[43] However, when the Zn^{2+} concentration is relatively high, Zn^{2+} induces increased ROS production, which in turn inhibits the mineralization of BMSCs.[44] In this study, the expression of the four genes mentioned above was measured using

Table 1. Blood parameters and liver and kidney function parameters of rats in each group at 4, 8, and 12 weeks post-surgery

Time (week)	Laboratory indicators	Blank	PCL	LZP	HZP	*p*-value
4	WBC (10^9/L)	11.28 ± 1.04	11.21 ± 1.49	11.35 ± 1.55	11.92 ± 1.43	$p = 0.9170$
	RBC (10^{12}/L)	8.16 ± 0.51	7.94 ± 0.71	7.53 ± 0.44	8.09 ± 0.44	$p = 0.5148$
	HB (g/L)	147.30 ± 7.64	143.00 ± 8.54	139.30 ± 13.01	144.00 ± 7.00	$p = 0.7755$
	PLT (10^9/L)	859.30 ± 230.90	863.00 ± 145.70	973.30 ± 137.60	944.30 ± 44.64	$p = 0.7453$
	ALT (U/L)	75.33 ± 17.62	97.00 ± 13.00	81.33 ± 15.63	75.33 ± 30.89	$p = 0.5530$
	AST (U/L)	243.30 ± 84.51	263.70 ± 42.10	210.30 ± 38.00	261.00 ± 65.82	$p = 0.2090$
	Urea (mmol/L)	6.84 ± 0.13	6.40 ± 0.37	6.90 ± 0.75	7.09 ± 1.04	$p = 0.6505$
	Cr (μmol/L)	32.33 ± 3.22	28.00 ± 3.46	31.33 ± 1.16	35.00 ± 3.61	$p = 0.1131$
8	WBC (10^9/L)	10.56 ± 0.33	10.91 ± 0.29	10.84 ± 1.49	10.08 ± 0.77	$p = 0.6545$
	RBC (10^{12}/L)	7.47 ± 1.28	7.90 ± 0.93	7.10 ± 1.16	6.71 ± 1.13	$p = 0.6243$
	HB (g/L)	134.70 ± 24.17	140.30 ± 9.24	130.70 ± 15.37	120.30 ± 18.90	$p = 0.5908$
	PLT (10^9/L)	879.30 ± 145.10	1092.00 ± 238.10	974.70 ± 207.40	1141.00 ± 153.70	$p = 0.3844$
	ALT (U/L)	89.67 ± 22.94	76.00 ± 7.00	75.33 ± 35.12	80.33 ± 46.48	$p = 0.9384$
	AST (U/L)	256.30 ± 12.01	264.30 ± 14.19	275.30 ± 50.96	246.00 ± 77.95	$p = 0.8901$
	Urea (mmol/L)	6.82 ± 0.18	5.97 ± 0.59	6.51 ± 0.64	6.29 ± 0.27	$p = 0.2248$
	Cr (μmol/L)	31.00 ± 3.61	32.33 ± 3.06	31.33 ± 2.31	33.67 ± 3.51	$p = 0.7368$
12	WBC (10^9/L)	10.75 ± 1.97	10.15 ± 0.77	10.05 ± 0.84	10.33 ± 0.43	$p = 0.8849$
	RBC (10^{12}/L)	7.92 ± 0.94	7.60 ± 1.28	7.36 ± 0.60	7.75 ± 0.49	$p = 0.8833$
	HB (g/L)	143.00 ± 11.27	138.30 ± 23.25	135.70 ± 16.04	142.30 ± 2.31	$p = 0.9240$
	PLT (10^9/L)	946.30 ± 84.24	1074.00 ± 226.80	988.00 ± 126.30	926.70 ± 131.40	$p = 0.6568$
	ALT (U/L)	83.67 ± 15.50	103.70 ± 13.32	89.33 ± 41.43	107.30 ± 47.35	$p = 0.7899$
	AST (U/L)	221.00 ± 14.73	234.70 ± 32.01	272.00 ± 55.22	257.30 ± 27.54	$p = 0.3593$
	Urea (mmol/L)	6.57 ± 0.77	5.72 ± 0.27	7.31 ± 0.49	6.53 ± 1.20	$p = 0.1715$
	Cr (μmol/L)	27.67 ± 1.53	33.33 ± 2.52	27.67 ± 3.51	31.67 ± 6.03	$p = 0.2385$

Note: Values are expressed in mean ± standard deviation.

Abbreviations: ALT: Alanine aminotransferase; AST: Aspartate aminotransferase; Cr: Creatinine; HB: Hemoglobin; HZP: High-density ZIF-8-coated PCL; LZP: Low-density ZIF-8-coated PCL; PCL: Polycaprolactone; PLT: Platelet; RBC: Red blood cell; WBC: White blood cell.

RT-qPCR (Figures 5 and 7). We found that the osteogenic activity of the LZP group was the most significant among the three groups. After 7 and 14 days of induction, the expression levels of osteogenesis-related genes in the LZP group were significantly upregulated compared to the corresponding time points in the PCL and HZP groups. The results indicate that the low-density ZIF-8 coating significantly enhances the osteogenic differentiation capacity of the scaffold. This may be mainly attributed to the fact that the Zn^{2+} concentration released by the LZP group better promotes osteogenic differentiation compared to the HZP group, which is consistent with previous research conclusions.

The immune microenvironment plays a crucial role in bone repair. A suitable immune microenvironment for osteogenic development can effectively promote bone regeneration, with macrophage phenotype being a key factor influencing bone formation and repair.[45,46] Macrophage phenotype transformation is a dynamic process; M1 and M2 phenotype macrophages can transform into each other under various stimuli.[47,48] The main function of the M1 type is to clear foreign bodies or pathogens in the early stage of injury or implantation, and to initiate the repair process, promoting an early inflammatory response to trauma. However, persistent M1 polarization can lead to immune rejection of implantation materials. The M2 type, on the other hand, mainly promotes inflammation resolution and bone tissue repair by secreting anti-inflammatory factors.[49,50] Therefore, the transformation of macrophage phenotype from M1 to M2 is extremely important for bone tissue repair. To explore whether the three scaffolds promote bone regeneration by regulating the immune microenvironment and influencing macrophage polarization, we co-cultured PCL, LZP, and HZP scaffolds with RAW264.7 cells *in vitro*. ELISA was used to detect macrophage polarization-related cytokines (IL-10, IL-12), and RT-qPCR was used to detect the expression of genes related to M1 macrophages (*Tnfa*, *Il1b*) and M2 macrophages (*Cd206*, *Arg1*). The results showed that IL-10 expression in the LZP group was significantly higher than that in the PCL and HZP groups, while IL-12 expression was lower than in the other two groups. The results of RT-qPCR detection of *Arg1*, *Tnfa*, *Cd206*, and *Il1b* are shown in Figure 6. The LZP group showed significantly higher levels of M2 macrophage-related genes than the PCL and HZP groups, while M1 macrophage-related genes were significantly lower ($p < 0.05$). This indicates that the LZP scaffold can better regulate the immune microenvironment, promote the transformation of macrophages from M1 to M2 phenotypes, and thus enhance bone regeneration capacity. Yi *et al.*[51] showed that Zn^{2+} can regulate the functional state of macrophages, induce macrophage polarization towards the M2 type with anti-inflammatory and tissue repair functions, help establish an anti-inflammatory microenvironment, and promote bone regeneration. To further investigate the ability of PCL, LZP, and HZP scaffolds to affect osteogenic capacity under immune regulation, changes in these two markers were further confirmed by ALP staining, Alizarin Red staining, and quantitative detection (Figures 5 and 7). The results showed that the low-density ZIF-8 coating suggests a potential relationship between the immune-regulated osteogenic capacity. The study shows that immune regulation creates the necessary microenvironment for osteogenic formation and determines the direction of subsequent regeneration processes. After macrophages are polarized to the M2 type through immune regulation, they secrete a series of regenerative cytokines. These factors collectively construct a microenvironment rich in osteogenic and angiogenic signals, laying the foundation for subsequent stem cell recruitment and differentiation, and also influencing key signaling pathways.[52] Studies by Shen *et al.*[53] have shown that factors such as BMP-2 secreted by M2 macrophages can activate the BMP/Smad signaling pathway in mesenchymal stem cells, upregulate the expression of key osteogenic genes such as *Runx2*, and promote osteogenic formation.

To further clarify the osteogenic capacity of the three scaffolds, this study constructed a rat skull defect model. Due to the high similarity between rats and humans in tissue structure, system function, and fracture healing mechanisms, rats are one of the most widely used and mature experimental animals in skull defect research.[54] The rat skull is flat and relatively large, facilitating standardized surgery for round bone defects. Previous studies have shown that the critical bone defect size in the rat skull is 5 mm in diameter, providing a suitable observation window for evaluating the osteogenic effect of bone repair materials.[55] Based on this, this study drilled full-thickness bone defects of approximately 5 mm in diameter on both sides of the sagittal suture in the rat skull. PCL, LZP, and HZP scaffolds were implanted at the defect site according to pre-grouped groups, while no scaffold was implanted in the control group. The repair effects of the three scaffolds on the critical-sized bone defect were investigated at 4, 8, and 12 weeks postoperatively.

Micro-CT is a technique that uses X-rays to generate high-resolution 3D images without damaging tissue. This allows us to observe the internal structure of specimens and reconstruct 3D images of bone defects, making it particularly suitable for the detection of new bone tissue in small animals.[56,57] Meanwhile, micro-CT not only provides images but also converts 3D images into objective bone

mass-related parameters. Among them, BV/TV and BMD are important quantitative indicators of micro-CT, which can directly reflect changes in bone mass.[58,59] To observe the repair effects of the three scaffolds on skull defects in rats, this study established a bilateral skull defect model in SD rats based on the stable characteristics of the SD rat population and the small individual differences. Micro CT was used to observe the growth of new bone in the bone defect area. Images were taken of the skull defects in each group of rats, and quantitative indicators such as new BV/TV and BMD were analyzed. Micro-CT 3D reconstruction images (**Figure 8**) showed that at 4, 8, and 12 weeks post-surgery, the bone repair effect was LZP group > PCL group > HZP group > blank group. The LZP group showed the best bone repair effect, with a statistically significant difference ($p < 0.05$). Furthermore, the BV/TV and BMD analysis results were consistent with the micro-CT results, further indicating that the LZP group had a better bone repair effect. In addition, histological staining (HE, Masson's) is a commonly used method for observing bone tissue growth, which can clearly show the bone tissue structure and cells in the bone marrow cavity.[60,61] To further verify the *in vivo* repair effect of the scaffold on bone defects, HE staining and Masson staining were performed on rat skull specimens from each group (Figure 9) to observe bone tissue structure. The HE staining results showed that at 4, 8, and 12 weeks post-surgery, the LZP group scaffold showed more bone tissue formation than the PCL group, HZP group, and blank control group. Masson staining results also indicated that the LZP group scaffold had a better osteogenic effect.

Immune regulation and angiogenesis play important roles in the repair of bone defects during bone tissue regeneration.[62] This study used a double immunofluorescence histochemical staining method to further investigate the immune regulation, osteogenic differentiation, and angiogenesis at the site of rat skull defects (Figure 10). Regarding immune regulation, iNOS and CD163 were polarization markers for macrophage M1 and M2 types, respectively.[63,64] Immunofluorescence staining results showed that the LZP scaffold significantly upregulated the expression of CD163, a marker of M2 macrophages, while downregulating the expression of iNOS, a marker of M1 macrophages. This indicates that the LZP scaffold can promote macrophage polarization from M1 to M2, thereby promoting bone defect repair. Regarding bone repair, BMP2 is a growth factor that regulates bone development and regeneration. It can induce undifferentiated BMSCs to differentiate into osteoblasts and promote osteoblast maturation, thereby accelerating bone regeneration.[36] In this study, the LZP scaffold showed higher levels of *Bmp2* expression at the defect site, indicating its strong ability to induce osteogenic differentiation. Furthermore, angiogenesis and bone tissue repair and remodeling are closely related processes, and the expression level of VEGF is closely associated with angiogenesis.[65] Immunofluorescence staining results showed that the LZP scaffold effectively promoted VEGF expression, superior to the PCL and HZP groups. This indicates that the LZP scaffold can more effectively promote angiogenesis *in vivo*. Therefore, the LZP scaffold appears to regulate macrophage polarization from M0 to M2. The polarized M2 macrophages upregulate the secretion of anti-inflammatory factors such as IL-10, ARG-1, CD206, and CD163, while downregulating pro-inflammatory factors such as IL-12, IL-1β, TNF-α, and iNOS, thereby creating an immune microenvironment beneficial to osteogenic formation. On the one hand, it directly stimulates the proliferation and differentiation of osteoblasts through the recruitment and proliferation of MSCs, and upregulates the expression of osteogenesis-related genes and proteins such as BMP-2, COL-1, ALP, and RUNX2. On the other hand, the upregulation of VEGF expression in the immune microenvironment stimulates vascular endothelial cells and drives angiogenesis. The synergistic effect of immune regulation and angiogenesis jointly enhances bone regeneration. (Figures 6, 10, and 12)

This study has several limitations. First, the release behavior of Zn^{2+} was evaluated in PBS solution rather than directly measured in the cellular culture microenvironment; therefore, the actual bioactive concentration of Zn^{2+} surrounding the cells remains unclear. In addition, although the present findings reveal a correlation between ZIF-8 coating density, Zn^{2+} release behavior, macrophage polarization, and osteogenic effects, the current research mainly demonstrates correlations and has not yet established clear causal mechanisms for osteogenic immunomodulation. Future studies involving signal pathway analysis, Zn^{2+} chelation, macrophage depletion/inhibition, or genetic approaches are needed to verify the underlying mechanisms. Moreover, while various surface modification strategies for PCL have been reported previously, this work primarily aims to indicate that within the ZIF-8 modification system, coating density may influence biological responses, rather than to establish that this method is universally superior to other surface engineering approaches. Furthermore, the *in vivo* evaluation in this study was limited to a rat calvarial defect model and did not include assessments of critical-sized defects, infected bone defects, or large animal models. Future investigations exploring these aspects would help to further clarify the clinical translation potential of this strategy.

In summary, this study prepared 3D-printed PCL scaffolds with different ZIF-8 density coatings. Compared with pure PCL scaffolds, the low-density ZIF-8-coated scaffolds exhibited better biocompatibility, effectively promoting the expression of bone tissue markers, regulating the immune microenvironment, promoting angiogenesis and bone defect repair, and showing good repair effects on rat skull defects, demonstrating good bone repair potential. This can provide a preliminary experimental reference for research on bone defect repair materials. However, this study only preliminarily explored the repair effect on rat skull defects. Whether it has good repair capabilities for other sites and larger volumes, or even large segments of bone defects, the mechanism of bone defect repair still needs further in-depth research.

5. Conclusion

This study fabricated 3D-printed PCL scaffolds featuring varying ZIF-8 coating densities and systematically evaluated their physicochemical properties as well as their efficacy in osteogenic repair. The results demonstrated that the LZP scaffold achieved a more favorable balance between biocompatibility and bone regeneration capacity, exhibiting superior bone repair outcomes in a rat cranial defect model. These findings suggest that LZP may establish a more conducive microenvironment for Zn^{2+} release, which is associated with the modulation of macrophage polarization and the enhancement of osteogenesis-related phenotypes, thereby fostering an osteoimmune microenvironment that is more favorable for bone regeneration. Overall, this study indicates that ZIF-8 coating density may be a critical factor influencing the biological performance of MOF-modified PCL scaffolds, providing an experimental basis for the further optimization of MOF-based surface-functionalized scaffolds in the field of bone tissue engineering.

Acknowledgments

None

Funding

This study was supported by the National Natural Science Foundation of China (32571583), the Guangdong Province Science and Technology Plan Project (2024A1515012265), the Zunyi City Science & Technology Innovation Talent Project (No. [2024] 04), and the GDAS Project of Science and Technology Development (2023GDASZH-2023010102).

Conflict of interest

The authors declare that they have no known competing financial interests.

Author contribution

Conceptualization: Jiaxiang Song, Qingde Wa
Data curation: Yuanhao Lv
Formal analysis: Guangquan Zhao
Funding acquisition: Weikang Xu, Qingde Wa
Investigation: Qianyu Xie
Methodology: Qianyu Xie, Xusihong Cai, Guangquan Zhao, Hao Tang
Resources: Guangquan Zhao
Software: Qianyu Xie, Hao Tang
Supervision: Shuai Huang, Weikang Xu, Qingde Wa
Validation: Qianyu Xie, Xusihong Cai, Hao Tang
Visualization: Yuanhao Lv, Jiaxiang Song
Writing–original draft: Qianyu Xie
Writing–review & editing: Shuai Huang, Weikang Xu, Qingde Wa

Ethics approval and consent to participate

All experimental protocols associated with animals in this study were approved by the Medical Ethics Committee of Zunyi Medical University (Approval No.: ZMU21-2412-016), and all methods were carried out in accordance with ARRIVE guidelines and regulations (the anesthesia method used in this study was intramuscular injection of xylazine hydrochloride). The euthanasia method (cervical dislocation performed under deep anesthesia) complied with AVMA guidelines.

Consent for publication

Not applicable.

Availability of data

All data generated or analyzed during this study are included in this published article.

References

1. Zhao Y, Wang J, Xu L, *et al*. Beyond Bone Loss: A Biology Perspective on Osteoporosis Pathogenesis, Multi-Omics Approaches, and Interconnected Mechanisms. *Biomedicines*. 2025;13(6):1443.

   doi: 10.3390/biomedicines13061443

2. Zhang Y, Wang Y, Ning X, *et al*. Guided Bone Regeneration Membrane Materials Loaded with Chimeric Nanovesicles Promote Early Bone Defect Regeneration. *Adv Healthc Mater*. 2025;14(32):e01323.

   doi: 10.1002/adhm.202501323

3. Gillman CE, Jayasuriya AC. FDA-approved bone grafts and bone graft substitute devices in bone regeneration. *Mater Sci Eng C Mater Biol Appl*. 2021;130:112466.

   doi: 10.1016/j.msec.2021.112466

4. Zhang J, Li S, He H, *et al*. Clinical guidelines for indications, techniques, and complications of autogenous bone grafting. *Chin Med J (Engl)*. 2024;137(1):5-7.

doi: 10.1097/CM9.0000000000002691

5. Hofmann GH, Sarsour R, Deursen WV, *et al*. Immune rejection of orthopedic tissue allograft scoping review: Are we missing a cause of graft/procedural failure? Current concepts. *J ISAKOS*. 2025;15:101002.

doi: 10.1016/j.jisako.2025.101002

6. Łuczak JW, Palusińska M, Matak D, *et al*. The Future of Bone Repair: Emerging Technologies and Biomaterials in Bone Regeneration. *Int J Mol Sci*. 2024;25(23):12766.

doi: 10.3390/ijms252312766

7. Xu C, Cheng P, Wang J, *et al*. Unveiling the Power of Magnetic-Driven Regenerative Medicine: Bone Regeneration and Functional Reconstruction. *Research (Wash D C)*. 2025;8:0707.

doi: 10.34133/research.0707

8. Przekora A, Kazimierczak P, Wojcik M. *Ex vivo* determination of chitosan/curdlan/hydroxyapatite biomaterial osseointegration with the use of human trabecular bone explant: New method for biocompatibility testing of bone implants reducing animal tests. *Mater Sci Eng C Mater Biol Appl*. 2021;119:111612.

doi: 10.1016/j.msec.2020.111612

9. Filip Ionescu OL, Mocanu AG, Neacşu IA, Ciocîlteu MV, Rău G, Neamţu J. Biocompatibility Studies on a Collagen-Hydroxyapatite Biomaterial. *Curr Health Sci J*. 2022;48(2):217-225.

doi: 10.12865/CHSJ.48.02.12

10. Zhang M, Wan B, Sun M, *et al*. Harnessing Immunomodulation: How Calcium Phosphate Biomaterials Orchestrate Bone Regeneration. *Tissue Eng Part A*. Published online June 24, 2025.

doi: 10.1089/ten.tea.2025.0091

11. Jin C, Liang J, Wu J, *et al*. Temporal Immunomodulatory Hydrogel Regulating the Immune-Osteogenic Cascade for Infected Bone Defects Regeneration. *Adv Mater*. 2026;38(2):e14419.

doi: 10.1002/adma.202514419

12. Qin D, Zhao Y, Cheng R, *et al*. Mussel-inspired immunomodulatory and osteoinductive dual-functional hydroxyapatite nanoplatform for promoting bone regeneration. *J Nanobiotechnology*. 2024;22(1):320.

doi: 10.1186/s12951-024-02593-3

13. Chen K, Luo L, Tao R, *et al*. 3D-Printed PCL/SrHA@DFO Bone Tissue Engineering Scaffold with Bone Regeneration and Vascularization Function. *ACS Appl Bio Mater*. 2025;8(2):1684-1698.

doi: 10.1021/acsabm.4c01866

14. Shen S, Shu B, Xu Y, *et al*. Characterization and Biocompatibility Assessment of 3D-Printed HA/PCL Porous Bionic Bone Scaffold: *in Vitro* and *in Vivo* Evaluation. *J Musculoskelet Neuronal Interact*. 2025;25(1):119-132.

doi: 10.22540/JMNI-25-119

15. Deshpande MV, Girase A, King MW. Degradation of Poly(ε-caprolactone) Resorbable Multifilament Yarn under Physiological Conditions. *Polymers (Basel)*. 2023;15(18):3819.

doi: 10.3390/polym15183819

16. Robles KN, Zahra FT, Mu R, Giorgio T. Advances in Electrospun Poly(ε-caprolactone)-Based Nanofibrous Scaffolds for Tissue Engineering. *Polymers (Basel)*. 2024;16(20):2853.

doi: 10.3390/polym16202853

17. Huang K, Li Q, Liu Y, *et al*. 3D-printed functionalized strontium-silk fibroin-hydroxyapatite scaffolds facilitate bone regeneration via immunomodulatory and sequential angiogenic-osteogenic coupling. *Bioact Mater*. 2025;55:271-289.

doi: 10.1016/j.bioactmat.2025.09.033

18. Mousavi Nejad Z, Zamanian A, Saeidifar M, Vanaei HR, Salar Amoli M. 3D Bioprinting of Polycaprolactone-Based Scaffolds for Pulp-Dentin Regeneration: Investigation of Physicochemical and Biological Behavior. *Polymers (Basel)*. 2021;13(24):4442.

doi: 10.3390/polym13244442

19. Itatani M, Német N, Valletti N, *et al*. Synthesis of Zeolitic Imidazolate Framework-8 Using Glycerol Carbonate. *ACS Sustain Chem Eng*. 2023;11(35):13043-13049.

doi: 10.1021/acssuschemeng.3c02876

20. Ejeian F, Razmjou A, Nasr-Esfahani MH, *et al*. ZIF-8 Modified Polypropylene Membrane: A Biomimetic Cell Culture Platform with a View to the Improvement of Guided Bone Regeneration. *Int J Nanomedicine*. 2020;15:10029-10043.

doi: 10.2147/IJN.S269169

21. Chen J, Zhang X, Huang C, *et al*. Osteogenic activity and antibacterial effect of porous titanium modified with metal-organic framework films. *J Biomed Mater Res A*. 2017;105(3):834-846.

doi: 10.1002/jbm.a.35960

22. Liu Y, Wang L, Dou X, *et al*. Osteogenesis or Apoptosis-Twofold Effects of Zn2+ on Bone Marrow Mesenchymal Stem Cells: An In Vitro and In Vivo Study. *ACS Omega*. 2024;9(9):10945-10957.

doi: 10.1021/acsomega.3c10344

23. Tian X, Zhang P, Xu J. Incorporating zinc ion into titanium surface promotes osteogenesis and osteointegration in implantation early phase. *J Mater Sci Mater Med*. 2023;34(11):55.

    doi: 10.1007/s10856-023-06751-1

24. Lin J, Huang L, Ou H, Chen A, Xiang R, Liu Z. Effects of ZIF-8 MOFs on structure and function of blood components. *RSC Adv*. 2021;11(35):21414-21425.

    doi: 10.1039/d1ra02873a

25. Si Y, Li X, Dong S, *et al*. Hydrogel scaffold encapsulating MSC-Exos and ZIF-8 promotes bone regeneration via coordinating osteogenesis and immunomodulation. *Bioact Mater*. 2025;54:329-351.

    doi: 10.1016/j.bioactmat.2025.08.026

26. Johari SA, Sarkheil M, Veisi S. Cytotoxicity, oxidative stress, and apoptosis in human embryonic kidney (HEK293) and colon cancer (SW480) cell lines exposed to nanoscale zeolitic imidazolate framework 8 (ZIF-8). *Environ Sci Pollut Res Int*. 2021;28(40):56772-56781.

    doi: 10.1007/s11356-021-14636-5

27. Yang C, Wen J, Xue Z, Yin X, Li Y, Yuan L. The accumulation and toxicity of ZIF-8 nanoparticles in Corbicula fluminea. *J Environ Sci (China)*. 2023;127:91-101.

    doi: 10.1016/j.jes.2022.03.020

28. Zhang X, Zhang X, Li Y, Zhang Y. Applications of Light-Based 3D Bioprinting and Photoactive Biomaterials for Tissue Engineering. *Materials (Basel)*. 2023;16(23):7461.

    doi: 10.3390/ma16237461

29. Wang T, Yang X, Qi X, Jiang C. Osteoinduction and proliferation of bone-marrow stromal cells in three-dimensional poly (ε-caprolactone)/ hydroxyapatite/collagen scaffolds. *J Transl Med*. 2015;13:152.

    doi: 10.1186/s12967-015-0499-8

30. Zhong L, Chen J, Ma Z, *et al*. 3D printing of metal-organic framework incorporated porous scaffolds to promote osteogenic differentiation and bone regeneration. *Nanoscale*. 2020;12(48):24437-24449.

    doi: 10.1039/d0nr06297a

31. Wang Z, Fu Q, Xie D, Wang F, Zhang G, Shan H. Facile Fabrication of Zeolitic Imidazolate Framework-8@ Regenerated Cellulose Nanofibrous Membranes for Effective Adsorption of Tetracycline Hydrochloride. *Molecules*. 2024;29(17):4146.

    doi: 10.3390/molecules29174146

32. Zhao J, Fan R, Xiang S, Hu J, Zheng X. Preparation and Lithium-Ion Separation Property of ZIF-8 Membrane with Excellent Flexibility. *Membranes (Basel)*. 2023;13(5):500.

    doi: 10.3390/membranes13050500

33. Mateu-Sanz M, Fuenteslópez CV, Uribe-Gomez J, *et al*. Redefining biomaterial biocompatibility: challenges for artificial intelligence and text mining. *Trends Biotechnol*. 2024;42(4):402-417.

    doi: 10.1016/j.tibtech.2023.09.015

34. Frazão LP, Vieira de Castro J, Neves NM. In Vivo Evaluation of the Biocompatibility of Biomaterial Device. In: *Advances in Experimental Medicine and Biology*. Vol 1250. Singapore: Springer; 2020:109-124.

    doi: 10.1007/978-981-15-3262-7_8

35. Hernández-Cubas LL, Sánchez-Moreno P, Capasso A, *et al*. Laser-Induced Graphene Interfaces with Controlled Electrical Conductivity, Topography and Wettability for Biomedical Applications. *ACS Appl Nano Mater*. 2025;8(51):24610-24622.

    doi: 10.1021/acsanm.5c05398

36. Nelson CL, Castellion CA, Humpal AP, *et al*. Glycosaminoglycan-Inspired Polymer Brushes Promote Human Mesenchymal Stem Cell Proliferation While Retaining Trilineage Differentiation Potential. *ACS Appl Mater Interfaces*. 2026;18(3):4952-4966.

    doi: 10.1021/acsami.5c23781

37. Na W, Kang MK, Park SH, *et al*. Aesculetin Accelerates Osteoblast Differentiation and Matrix-Vesicle-Mediated Mineralization. *Int J Mol Sci*. 2021;22(22):12391.

    doi: 10.3390/ijms222212391

38. Bernar A, Gebetsberger JV, Bauer M, Streif W, Schirmer M. Optimization of the Alizarin Red S Assay by Enhancing Mineralization of Osteoblasts. *Int J Mol Sci*. 2022;24(1):723.

    doi: 10.3390/ijms24010723

39. Wytrwal-Sarna M, Sekuła-Stryjewska M, Pomorska A, *et al*. The Effect of the Topmost Layer and the Type of Bone Morphogenetic Protein-2 Immobilization on the Mesenchymal Stem Cell Response. *Int J Mol Sci*. 2022;23(16):9287.

    doi: 10.3390/ijms23169287

40. Park KR, Kim S, Cho M, Yun HM. Limonoid Triterpene, Obacunone Increases Runt-Related Transcription Factor 2 to Promote Osteoblast Differentiation and Function. *Int J Mol Sci*. 2021;22(5):2483.

    doi: 10.3390/ijms22052483

41. Ansari S, Ito K, Hofmann S. Alkaline Phosphatase Activity of Serum Affects Osteogenic Differentiation Cultures. *ACS Omega*. 2022;7(15):12724-12733.

    doi: 10.1021/acsomega.1c07225

42. Akhir HM, Teoh PL. Collagen type I promotes osteogenic differentiation of amniotic membrane-derived mesenchymal stromal cells in basal and induction media. *Biosci Rep*. 2020;40(12):BSR20201325.

doi: 10.1042/BSR20201325

43. Yuan X, Wu T, Lu T, Ye J. Si and Zn dual ions upregulate the osteogenic differentiation of mBMSCs: mRNA transcriptomic sequencing analysis. *J Mater Sci Mater Med*. 2024;35(1):54.

doi: 10.1007/s10856-024-06825-8

44. Balogh E, Tóth A, Csiki DM, Jeney V. Zinc Ameliorates High Pi and Ca-Mediated Osteogenic Differentiation of Mesenchymal Stem Cells. *Nutrients*. 2024;16(23):4012.

doi: 10.3390/nu16234012

45. Weitzmann MN. Bone and the Immune System. *Toxicol Pathol*. 2017;45(7):911-924.

doi: 10.1177/0192623317735316

46. He J, Chen G, Liu M, *et al*. Scaffold strategies for modulating immune microenvironment during bone regeneration. *Mater Sci Eng C Mater Biol Appl*. 2020;108:110411.

doi: 10.1016/j.msec.2019.110411

47. Xu Z, Wu L, Tang Y, *et al*. Spatiotemporal Regulation of the Bone Immune Microenvironment via Dam-Like Biphasic Bionic Periosteum for Bone Regeneration. *Adv Healthc Mater*. 2023;12(1):e2201661.

doi: 10.1002/adhm.202201661

48. Li M, Chu X, Wang D, *et al*. Tuning the surface potential to reprogram immune microenvironment for bone regeneration. *Biomaterials*. 2022;282:121408.

doi: 10.1016/j.biomaterials.2022.121408

49. Zhang F, Lv M, Wang S, *et al*. Ultrasound-triggered biomimetic ultrashort peptide nanofiber hydrogels promote bone regeneration by modulating macrophage and the osteogenic immune microenvironment. *Bioact Mater*. 2023;31:231-246.

doi: 10.1016/j.bioactmat.2023.08.008

50. Lin X, Liu C, Lei Y, *et al*. Cichoric acid-loaded hydroxyapatite nanorods remodel the immune microenvironment to enhance bone regeneration. *Phytomedicine*. 2026;150:157701.

doi: 10.1016/j.phymed.2025.157701

51. Yi L, Tang R, Shao C, *et al*. A Biodegradable Zinc Alloy Membrane with Regulation of Macrophage Polarization for Early Vascularized Bone Regeneration. *Biomater Res*. 2025;29:0223.

doi: 10.34133/bmr.0223

52. Zheng H, Yan P, Liu P, *et al*. Ultrasound-activated piezoelectric scaffolds target dual Ca2+/NF-κB signaling pathways to orchestrate immunomodulation and osteogenesis for accelerated bone regeneration. *Mater Today Bio*. 2025;35:102299.

doi: 10.1016/j.mtbio.2025.102299

53. Shen H, Shi J, Zhi Y, *et al*. Improved BMP2-CPC-stimulated osteogenesis in vitro and in vivo via modulation of macrophage polarization. *Mater Sci Eng C Mater Biol Appl*. 2021;118:111471.

doi: 10.1016/j.msec.2020.111471

54. Parco TM, Wagner JD, Parbhoo P, *et al*. Comprehensive evaluation of critical-size calvarial defect in athymic rat model. *Front Physiol*. 2025;16:1662424.

doi: 10.3389/fphys.2025.1662424

55. Banu SA, Manjusha KM, Mamachan M, Sharun K. From flat bones to functional healing: redefining rodent calvarial defect models for translational bone regeneration research. *Ann Med Surg (Lond)*. 2025;87(10):6382-6385.

doi: 10.1097/MS9.0000000000003528

56. Griesbach JK, Schulte FA, Schädli GN, Rubert M, Müller R. Mechanoregulation analysis of bone formation in tissue engineered constructs requires a volumetric method using time-lapsed micro-computed tomography. *Acta Biomater*. 2024;179:149-163.

doi: 10.1016/j.actbio.2024.03.008

57. Timmerman G, Van Goethem A, Docter D, *et al*. Evaluating micro-computed tomography for investigation of the pediatric hyoid-larynx complex. *Pediatr Radiol*. 2025;55(10):2138-2147.

doi: 10.1007/s00247-025-06364-6

58. Song D, Xu P, Liu S, Wu S. Dental pulp stem cells expressing SIRT1 improve new bone formation during distraction osteogenesis. *Am J Transl Res*. 2019;11(2):832-843.

59. Seo SJ, Lim JH, Lee Y, Bark CW, Kim YG. High-Throughput Analysis of New Bone Formation and Bone Substitutes After Maxillary Sinus Floor Elevation Using Synchrotron Radiation Micro-Computed Tomography. *J Nanosci Nanotechnol*. 2019;19(2):680-686.

doi: 10.1166/jnn.2019.15906

60. Su Y, Ye B, Zeng L, *et al*. Small Intestinal Submucosa Biomimetic Periosteum Promotes Bone Regeneration. *Membranes (Basel)*. 2022;12(7):719.

doi: 10.3390/membranes12070719

61. Yang Y, Chen D, Li Y, *et al*. Effect of Puerarin on Osteogenic Differentiation in vitro and on New Bone Formation in vivo. *Drug Des Devel Ther*. 2022;16:2885-2900.

doi: 10.2147/DDDT.S379794

62. Yuan Y, Xu Y, Mao Y, *et al*. Three Birds, One Stone: An Osteo-Microenvironment Stage-Regulative Scaffold for Bone Defect Repair through Modulating Early Osteo-Immunomodulation, Middle Neovascularization, and Later Osteogenesis. *Adv Sci (Weinh)*. 2024;11(6):e2306428.

doi: 10.1002/advs.202306428

63. Chavanisakun C, Keawvichit R, Benjakul N. M1 and M2 Macrophage Polarization Correlates with Activity and Chronicity Indices in Lupus Nephritis. *Life (Basel)*. 2025;15(1):55.

doi: 10.3390/life15010055

64. Xu J, Chen X, Zhang H, *et al*. Platelet-rich plasma relieves inflammation and pain by regulating M1/M2 macrophage polarization in knee osteoarthritis rats. *Sci Rep*. 2025;15(1):12805.

doi: 10.1038/s41598-025-97501-6

65. Lee JB, Hong JY, Shim H, *et al*. Bone morphogenetic protein-2-derived osteogenic peptide promotes bone regeneration via osteoblastogenesis. *Regen Ther*. 2025;30:911-919.

doi: 10.1016/j.reth.2025.09.006